Astronomy & Astrophysics manuscript no. freundlich_phibss2
December 21, 2018

PHIBSS2: survey design and $z = 0.5 - 0.8$ results. Molecular gas reservoirs during the winding-down of star formation.

J. Freundlich[1,2,3,⋆], F. Combes[1,2], L. J. Tacconi[4], R. Genzel[4,5,6], S. Garcia-Burillo[7], R. Neri[8], T. Contini[9], A. Bolatto[10], S. Lilly[11], P. Salomé[1], I. C. Bicalho[1], J. Boissier[8], F. Boone[9], N. Bouché[9], F. Bournaud[12], A. Burkert[13], M. Carollo[11], M. C. Cooper[14], P. Cox[15], C. Feruglio[16], N. M. Förster Schreiber[6], S. Juneau[12], M. Lippa[6], D. Lutz[6], T. Naab[17], A. Renzini[18], A. Saintonge[19], A. Sternberg[20], F. Walter[21], B. Weiner[22], A. Weiß[23], and S. Wuyts[24]

(Affiliations can be found after the references)

Received XXX; accepted YYY

ABSTRACT

Following the success of the Plateau de Bure high-z Blue Sequence Survey (PHIBSS), we present the PHIBSS2 legacy program, a survey of the molecular gas properties of star-forming galaxies on and around the star formation main sequence (MS) at different redshifts using IRAM's NOrthern Extended Millimeter Array (NOEMA). This survey significantly extends the existing sample of star-forming galaxies with CO molecular gas measurements, probing the peak epoch of star formation ($z = 1 - 1.6$) as well as its building-up ($z = 2 - 3$) and winding down ($z = 0.5 - 0.8$). The targets are drawn from the well-studied GOODS, COSMOS and AEGIS cosmological deep fields and uniformly sample the MS in the stellar mass ($M_\star$) - star formation rate (SFR) plane with $\log(M_\star/M_\odot) = 10 - 11.8$ and $SFR = 3.5 - 500\ M_\odot yr^{-1}$ without morphological selection, thus providing a statistically meaningful census of star-forming galaxies at different epochs. We describe the survey strategy and sample selection before focusing on the results obtained at redshift $z = 0.5 - 0.8$, where we report 60 CO(2-1) detections out of 61 targets. We determine molecular gas masses between 2.10^9 and $5.10^{10}\ M_\odot$ and separately obtain disk sizes and bulge-to-total (B/T) luminosity ratios from HST I-band images. The median molecular gas-to-stellar mass ratio $\widetilde{\mu_{gas}} = 0.28 \pm 0.04$, gas fraction $\widetilde{f_{gas}} = 0.22 \pm 0.02$ and depletion time $\widetilde{t_{depl}} = 0.84 \pm 0.07$ Gyr as well as their dependence with stellar mass and offset from the MS follow the scaling relations obtained by Tacconi et al. (2018) for a much larger sample of galaxies spanning a significantly wider range of redshifts, the cosmic evolution of the SFR being mainly driven by that of the molecular gas fraction. The galaxy-averaged molecular Kennicutt-Schmidt (KS) relation between molecular gas and SFR surface densities is strikingly linear, pointing towards similar star formation timescales within galaxies at any given epoch. In terms of morphology, the molecular gas content, the SFR as well as the disk stellar mass and molecular gas fraction do not seem to correlate with B/T and the stellar surface density, which suggests an ongoing supply of fresh molecular gas to compensate for the build-up of the bulge. Our measurements do not yield any significant variation of the depletion time with B/T and hence no strong evidence for morphological quenching within the scatter of the MS.

Key words. Galaxies: evolution – Galaxies: high redshift – Galaxies: star formation – Galaxies: ISM – ISM: molecules

1. Introduction

The main sequence of star formation

Observed massive galaxies in the distant Universe form stars at much higher rates than their local counterparts, with a peak epoch of star formation between $z = 1 - 3$ (Noeske et al. 2007; Daddi et al. 2007; Reddy & Steidel 2009; Bouwens et al. 2010; Cucciati et al. 2012; Lilly et al. 2013; Madau & Dickinson 2014). At each epoch, there is a bimodality between red passive galaxies on one side and blue star-forming galaxies on the other, most of the latter lying on a relatively tight, almost linear relation between their stellar mass ($M_\star$) and star formation rate (SFR), known as the star formation 'main sequence' (MS; Baldry et al. 2004; Brinchmann et al. 2004; Noeske et al. 2007; Elbaz et al. 2007, 2011; Daddi et al. 2007; Schiminovich et al. 2007; Damen et al. 2009; Santini et al. 2009; Rodighiero et al. 2010, 2011; Peng et al. 2010b; Wuyts et al. 2011b; Sargent et al. 2012; Whitaker et al. 2012, 2014; Speagle et al. 2014; Renzini & Peng 2015; Schreiber et al. 2015). About 90% of the cosmic star formation history since $z = 2.5$ took place near this MS. The ≤ 0.3 dex scatter of the MS, the rotating disk morphology of most galaxies that constitute it (Förster Schreiber et al. 2006, 2009; Genzel et al. 2006, 2008; Stark et al. 2008; Daddi et al. 2010a; Wuyts et al. 2011b) and the long star formation cycles inferred from the number of star-forming galaxies observed between $z = 1 - 2$ (Daddi et al. 2005, 2007; Caputi et al. 2006) argue in favor of a relatively smooth mode of star formation. The large molecular gas reservoirs fueling star formation (Erb et al. 2006; Daddi et al. 2010a; Tacconi et al. 2010, 2013) are thought to be maintained by a continuous supply of fresh gas from the cosmic web and minor mergers (Birnboim & Dekel 2003; Kereš et al. 2005, 2009; Dekel & Birnboim 2006; Cattaneo et al. 2006; Ocvirk et al. 2008; Dekel et al. 2009a; Genel et al. 2010). Typical star-forming galaxies are expected to progress along the MS in a slowly evolving gas-regulated quasi equilibrium between inflows, outflows and star formation (Bouché et al. 2010; Davé et al. 2011b, 2012; Feldmann 2013; Lilly et al. 2013; Dekel et al. 2013; Peng & Maiolino 2014; Dekel & Mandelker 2014) until their star formation is quenched when they enter denser environments or grow past the Schechter mass ($M_\star \sim 10^{10.8-11} M_\odot$; Conroy & Wechsler 2009; Peng et al. 2010b), and then to rapidly transit down to the red sequence. Episodes of gas compaction, depletion and replenishment could confine them within the scatter of the MS before the final quenching occurs (Dekel & Burkert 2014; Zolotov et al. 2015; Tacchella et al. 2016a,b). Quenching might be due to a combination of factors including gas removal

⋆ e-mail: jonathan.freundlich@obspm.fr

by winds driven by supernovae or active galactic nuclei (AGN), gas streams from the cosmic web that stop penetrating galactic haloes above a critical halo mass, a sudden drop in the gas cooling, a change in morphology and/or environmental effects.

The equilibrium model predicts strong correlations between the specific star formation rate (sSFR = SFR/M_{star}) and the gas fraction (or equivalently, the gas-to-stellar mass ratio μ_{gas} = M_{gas}/M_{star}, where M_{gas} is either the total or the molecular gaseous mass of the galaxy) as they evolve with redshift, while the gas compaction scenario further implies gradients of the central gas density, gas fraction and depletion time (t_{depl} = M_{gas}/SFR) across the MS. Measurements of these quantities at different redshifts thus provide crucial observational tests to understand the building-up and the winding-down of normal MS star-forming galaxies. The depletion time, which measures the star formation efficiency (SFE), has notably been suggested to decrease with redshift up to $z = 1$ (Combes et al. 2011, 2013). The Kennicutt-Schmidt (KS) relation between the molecular gas and SFR surface densities, $\Sigma_{SFR} \propto (\Sigma_{gas})^N$, further characterizes the SFE averaged over entire galaxies or subregions within them. It has been shown to be near linear on galactic and subgalactic scales for $\Sigma_{gas} > 10$ $M_\odot pc^{-2}$, with an exponent $N = 0.9 - 1.3$ and a scatter of ±0.3 – 0.4 dex (Schmidt 1959; Kennicutt 1998b; Bigiel et al. 2008, 2011; Leroy et al. 2008, 2013; Daddi et al. 2010a,b; Saintonge et al. 2011a; Schruba et al. 2011; Kennicutt & Evans 2012), indicating relatively uniform molecular gas depletion times around 1 – 2 Gyr.

The PHIBSS survey up to now

The Plateau de Bure High-z Blue Sequence Survey (PHIBSS, PI: L. Tacconi & F. Combes) carried out at the IRAM Plateau de Bure interferometer (PdBI; Guilloteau et al. 1992; Cox 2011) aimed at better understanding the winding-down of star formation within normal MS star-forming galaxies from the point of view of their molecular gas reservoirs. It focused on the massive tail of the MS at $z = 1.2$ and 2.2, with $\log(M_\star/M_\odot) \geqslant 10.4$ and $\log(SFR/M_\odot yr^{-1}) \geqslant 1.5$, and comprised 52 CO (3-2) detections and 8 higher resolution imaging observations with beam sizes between $0.3'' - 1''$. It uncovered large molecular gas reservoirs, with mean molecular gas fractions $f_{gas} = M_{gas}/(M_{gas} + M_\star)$ of 33% at $z = 1.2$ and 47% at $z = 2.2$ (Tacconi et al. 2010, 2013), when they only reach 7-10% in local giant spirals (Leroy et al. 2008; Saintonge et al. 2011a), showing that the cosmic evolution of the SFR is mainly due to the diminishing molecular gas content. Tacconi et al. (2013) further showed that f_{gas} decreases with $M_\star$, which can be interpreted in terms of feedback models where the first generations of stars remove part of the gas or in terms of a mass dependence of the accretion or star formation efficiencies, since μ_{gas} = sSFR × t_{depl} (e.g., Bouché et al. 2010; Davé et al. 2011a). The PHIBSS also obtained a near linear KS relation lying in the continuity of low redshift measurements, albeit with a slightly lower mean depletion time (Genzel et al. 2010; Tacconi et al. 2013). The sub-arcsecond follow-up observations enabled to obtain good quality rotation curves and resolved velocity dispersion maps, showing an increased turbulent support compared to low redshift which is compatible with models where cosmic streams feed the disk and trigger violent gravitational instabilities (e.g., Dekel et al. 2009b). Resolved kinematics also enabled to separate smoothed ensembles of clumps due to their different velocities, and to obtain a resolved KS relation at sub-galactic scale for four galaxies of the sample (Freundlich et al. 2013). Genzel et al. (2013) further obtained a pixel by pixel KS relation for one typical z=1.53 massive star-forming galaxy from the PHIBSS sample.

The PHIBSS2 legacy program

Built on the success of the PHIBSS, the IRAM PHIBSS2 legacy program (PIs: F. Combes, S. García-Burillo, R. Neri & L. Tacconi) intends to extend these results to a wider range of redshifts and to better sample the $M_\star$-SFR plane at each redshift. This four year program was phased to optimize and exploit the NOrthern Extended Millimeter Array (NOEMA; Schuster 2014) capabilities as they came online at the PdBI, which enabled a significant statistical gain with the smaller integration times and the increased sensitivity. PHIBSS2 has measured mean molecular gas fractions and depletion times in different redshift bins and across the MS, with the aim of studying the connection between star formation and molecular gas reservoirs and its evolution with redshift. Genzel et al. (2015) and Tacconi et al. (2018) already use PHIBSS2 detections together with other measurements to quantify precisely how the depletion time and the gas fraction depend on redshift, stellar mass and the offset from the MS reference line. They notably find that while the gas fraction decreases steeply with time, the depletion time slowly increases. They show how the gas fraction progressively increases above the MS and decreases below and how the depletion time follows the opposite trend without depending much on the stellar mass.

In this paper, we present the PHIBSS2 strategy and its results at $z = 0.5 - 0.8$. In this redshift bin, we report 60 CO(2-1) detections within a sample of 61 star-forming galaxies, hence constituting the first systematic census of the molecular gas in this redshift range. This sample bridges the gap between observations of the molecular gas in the nearby Universe and at the peak epoch of star formation, probing the crucial period of the winding-down of star formation in the last 10 Gyr of the history of the Universe. Until now, the molecular gas content of galaxies in this redshift range had paradoxically not been as much studied as that of higher redshift galaxies, partly because the CO line flux increase with frequency makes high CO rotational transitions more easily observable at higher redshift (Combes et al. 1999). We determine the molecular gas content, the sizes and morphology of these galaxies and describe the star formation conditions within them in terms of gas fraction, depletion time and surface densities. Section 2 presents the general PHIBSS2 strategy, the sample selection and its implementation with the IRAM Plateau de Bure interferometer and its NOEMA upgrade. Section 3 reports the CO molecular gas measurements we obtain at $z = 0.5 - 0.8$ and the results of our morphological study. In section 4, we interpret our results in terms of molecular gas fraction and depletion time, their dependence on morphology and the KS relation. We conclude in section 5. Through this paper, we assume a flat ΛCDM Universe with $\Omega_m = 0.3$, $\Omega_\Lambda = 1 - \Omega_m$ and $H_0 = 70$ km.s^{-1}.Mpc^{-1}.

2. Observations

2.1. Survey goals and strategy

The PHIBSS2 4-year legacy program is designed as a comprehensive and systematic study of the CO molecular gas content of galaxies during the build-up ($z = 2 - 3$), peak ($z = 1 - 1.6$) and subsequent winding-down ($z = 0.5 - 0.8$) of star formation in the Universe. As shown Fig. 1, it targets more than 120 sources over three redshift bins sampling the $M_\star$-SFR plane in the well-studied GOODS-North, COSMOS and AEGIS cosmo-

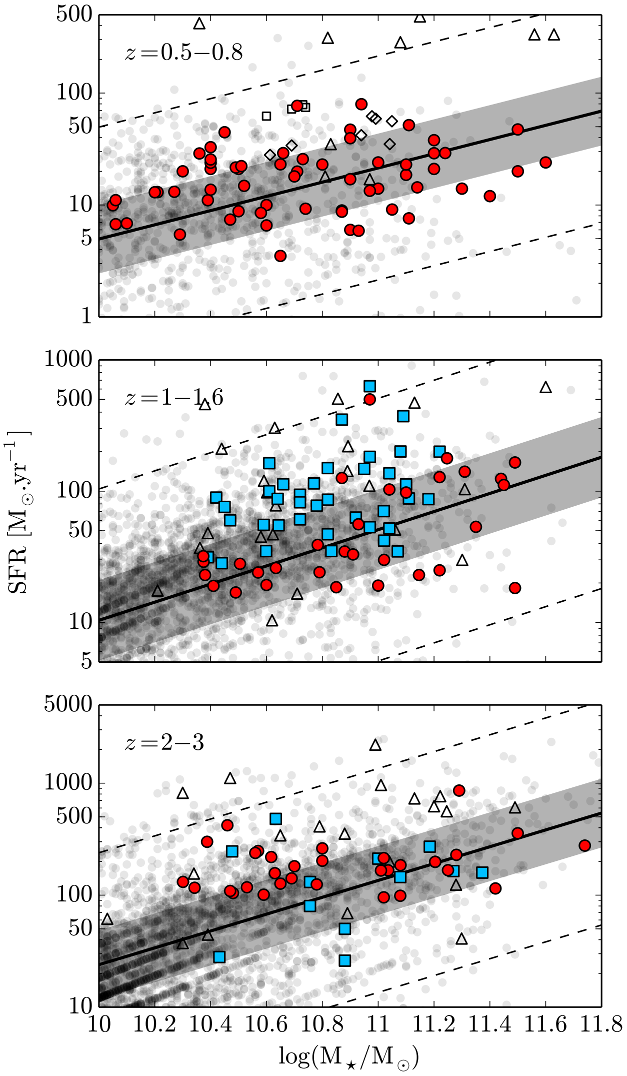

Fig. 1: Location of the PHIBSS2 sample in the three redshift ranges $z = 0.5 - 0.8$, $z = 1 - 1.6$ and $z = 2 - 3$ as a function of stellar mass $M_\star$ and SFR. The PHIBSS2 galaxies at $z = 0.5-0.8$ presented in this paper and the targets in the other redshift ranges are all marked as plain red circles. The PHIBSS sample (Tacconi et al. 2010, 2013) is indicated as plain blue squares while other existing CO measurements in the same redshift ranges are displayed as open triangles, including ULIRGs at $z = 0.5 - 0.8$ observed with the IRAM 30m telescope (Combes et al. 2011, 2013), near MS star-forming galaxies between $z = 0.5-3$ (Daddi et al. 2010a; Magdis et al. 2012b; Magnelli et al. 2012), above MS submillimeter galaxies between $z = 1.2 - 3$ (Greve et al. 2005; Tacconi et al. 2006, 2008; Bothwell et al. 2013) and lensed MS galaxies between $z = 1.2-3$ observed with the IRAM PdBI (Saintonge et al. 2013, and references therein), as well as additional sources between $z = 1 - 2.5$ observed with ALMA and NOEMA (Silverman et al. 2015; Decarli et al. 2016, Genzel et al. in prep.). The upper panel also shows sources observed by Geach et al. (2011) at $z \sim 0.4$ as open diamonds and Bauermeister et al. (2013) at $z \sim 0.5$ as open squares. The background data points correspond to 3D-HST galaxies in the AEGIS, GOODS-North, COSMOS and UDS fields (Brammer et al. 2012; Momcheva et al. 2016), while the solid line highlights the mean MS line from Speagle et al. (2014) in each redshift range. The shaded area corresponds to the 0.3 dex scatter of the MS and the dashed line to ±1 dex.

logical fields on and around the MS. It significantly expands the first PHIBSS sample, which focused on galaxies at $z = 1.2$ and 2.2, doubles the number of CO measurements available at $z > 2$, systematically probes the winding-down epoch at $z = 0.5 - 0.8$ and includes measurements below the MS at $z = 1 - 1.6$. The interconnected science goals of the PHIBSS2 survey are:

1. Following the evolution of the molecular gas fraction and the depletion time in normal MS star-forming galaxies at different epochs to establish quantitatively whether the evolution of the cosmic SFR is mostly driven by the available molecular gas reservoirs.

2. Characterizing the dependence of the gas fraction and the depletion time on the sSFR to compare the galaxy population on, above and below the MS. Quantifying this dependence will allow us to investigate whether "out of equilibrium" systems above the MS are fundamentally different from MS galaxies, how the quenching of star formation occurs below it and in future studies to estimate gas fractions and depletion times directly from SFR data.

3. Specifying the dependence of the gas fraction on the stellar mass to test feedback and quenching models. PHIBSS2 indeed enables to confirm and quantify the decrease of the gas fraction with stellar mass uncovered by PHIBSS, over a broader range of stellar masses $\log(M_\star/M_\odot) = 10 - 11.6$ spanning from the stellar feedback regime to the quenching regime.

4. Testing the impact of AGN, environment and morphology on quenching owing to a purely mass-selected sample above the Schechter mass. PHIBSS and PHIBSS2 together indeed provide a large enough sample of about 50 star-forming galaxies with $\log(M_\star/M_\odot) > 10.8$ to test how gas properties correlate with the presence of an AGN, environment and morphological indicators such as the bulge-to-total ratio and the stellar mass surface density.

5. Searching for molecular outflows to test stellar and AGN feedback models. While powerful galactic winds of ionized gas are found to be ubiquitous amongst star-forming galaxies at high-redshift (Pettini et al. 2000; Weiner et al. 2009; Genzel et al. 2011; Newman et al. 2012; Förster Schreiber et al. 2014), detecting molecular gas outflows is still challenging and often limited to nearby quasars and ultraluminous infrared galaxies (Feruglio et al. 2010; Sturm et al. 2011; Geach et al. 2014; Cicone et al. 2014). With more than 180 spectra from PHIBSS and PHIBSS2, we will be able to use deep stacking techniques to detect molecular outflows both in the stellar and in the AGN feedback regimes.

6. Determining the molecular gas distribution and kinematics from sub-arcsecond follow-ups of selected targets to establish spatially-resolved KS relations, rotation curves and velocity dispersion maps at different redshifts. In addition to galaxy-averaged measurements, PHIBSS2 indeed includes spatially resolved molecular gas observations of selected targets with NOEMA and ALMA that can be compared to the stellar, SFR and ionized gas distributions from complementary observations.

7. Probing the physical state of the gas from the CO line excitation at different $M_\star$, SFR and redshifts. Although recent observations (Ivison et al. 2011; Sharon et al. 2016; Dessauges-Zavadsky et al. 2017) indicate that the CO spectral energy distributions (SED) of star-forming galaxies at high-redshift are similar to but slightly more excited than that of the Milky Way, measurements are still scarce. The combined PHIBSS and PHIBSS2 sample will constitute a benchmark to investigate more systematically the gas excitation at high redshift with additional CO transitions. Follow-ups to probe dense gas tracers such as HCN will further help characterize the conditions ruling star formation.

The first three points are addressed in Genzel et al. (2015) and Tacconi et al. (2018), whose scope extends beyond the PHIBSS and PHIBSS2 programs as these articles use a wealth of molecular gas data, combining both CO and dust measurements in order to yield quantitative scaling relations for the molecular gas fraction and the depletion time and to eliminate concerns about the CO to molecular gas mass conversion factor. The PHIBSS2 program totalizes about 1068 hours on source at the IRAM NOEMA interferometer over four years, and participates in current efforts to better understand star-forming galaxies and their evolution. It is indeed one element among different large interconnected surveys, including KMOS-3D (Wisnioski et al. 2015), Large Binocular Telescope (LBT) LUCI spectroscopic observations (Wuyts et al. 2014), SINS/zC-SINF (Förster Schreiber et al. 2006, 2009, 2014; Genzel et al. 2006, 2011), MUSE imaging and kinematics (Contini et al. 2016), Hubble Space Telescope (HST) imaging with CANDELS (Grogin et al. 2011; Koekemoer et al. 2011) and 3D-HST grism spectroscopy (Brammer et al. 2012; Momcheva et al. 2016), many of these surveys drawing their samples from the same parent population.

2.2. Sample selection

The PHIBSS2 sample was drawn from large panchromatic imaging surveys with good spectroscopic redshifts and well-calibrated stellar masses, SFR and HST morphologies, namely the North field of the Great Observatories Origins Deep Survey (GOODS-N; R.A. = 12h36m, DEC. = 62°14′; Giavalisco et al. 2004), the Cosmic Evolution Survey (COSMOS; R.A. = 10h00m, DEC. = 02°12′; Scoville et al. 2007; Laigle et al. 2016) and the All-Wavelength Extended Groth Strip International Survey (AEGIS; R.A. = 14h17m, DEC. = 52°30′; Davis et al. 2007; Noeske et al. 2007). These three fields constitute well-understood parent samples with excellent multi-band ancillary data from the X-ray to the radio, which enables to quantitatively relate the PHIBSS2 sample to a much larger census of typical star-forming galaxies. Selected galaxies in the GOODS-N and AEGIS fields are part of the 3D-HST sample (Brammer et al. 2012; Momcheva et al. 2016) while those in the COSMOS field were taken from the zCOSMOS survey (Lilly et al. 2007, 2009). The stellar masses across the different parent samples are determined through spectral energy distribution (SED) modelling based on a Chabrier Initial Mass Function (IMF). Such modelling makes standard assumptions on the star formation histories and the dust attenuation within these galaxies (Erb et al. 2006; Förster Schreiber et al. 2009; Wuyts et al. 2011a). The SFR are estimated following a combination of UV and IR luminosities to account both for unobscured and dust-embedded star formation according to Eq. 1 of Wuyts et al. (2011a), based on Kennicutt (1998a) and corrected for a Chabrier IMF. The total IR luminosity is extrapolated from Spitzer 24 μm assuming a single luminosity independent FIR SED following Wuyts et al. (2008). The typical systematic uncertainties on both the stellar mass and the SFR are conservatively estimated at about 0.2 dex (e.g., Wuyts et al. 2011a; Whitaker et al. 2014; Roediger & Courteau 2015).

The PHIBSS2 targets are chosen to have deep HST imagery, high-quality spectroscopic redshifts, as well as good rest-frame UV and Herschel PACS and/or 24 μm observations for the SFR estimate. We aimed at a homogeneous coverage of the MS and its scatter in the $M_\star$-SFR plane, with $\log(M_\star/M_\odot) \geq 10.1$ and SFR $\geq 3.5\ M_\odot yr^{-1}$ to assure a high probability of detection for reasonable on-source integration times. As shown in Fig. 1, this coverage excludes the lower mass end of the MS but fully covers the MS above the cuts in stellar mass and SFR. We applied no morphological selection and the relatively high masses surveyed ensure that the selected galaxies have metallicities close to solar metallicity, which minimizes the metallicity-induced variations of the CO to molecular gas mass conversion factor. We further selected galaxies with Hα and, when possible, Hβ and [OIII] emission free from atmospheric line contamination for ionized gas kinematics and metallicity determinations. Considering Poisson errors and our past experience with PHIBSS, we required at least 10 measurements in any given part of the parameter space, for example below $\log(M_\star/M_\odot) = 10.4$ at $z = 0.5 - 0.8$ or above the Schechter mass in each redshift bin, to establish well-determined average gas fraction and depletion time. As shown by Tacconi et al. (2018) in their Appendix, establishing the redshift, MS-offset and stellar mass dependencies of the gas fraction and depletion time requires at least 40 sources in more than two redshift slices and a coverage over 1 dex both in stellar mass and MS-offset. Such constraints on the sample size further allow us to test the impact of AGN and environment, as we can split the sample into mass-matched sub-samples with an expected AGN fraction of 25–50% (Mullaney et al. 2012; Juneau et al. 2013) while 20 to 30 % of the targets display interacting satellites.

2.3. Implementation with the NOEMA interferometer

The CO observations were carried out between June 2014 and June 2017 with the IRAM Plateau de Bure millimeter interferometer and its NOEMA upgrade (Guilloteau et al. 1992; Cox 2011; Schuster 2014). The interferometer comprised six 15 m antennas at the beginning of the project and was upgraded to seven and eight antennas in September 2014 and April 2016, which enabled to reach higher sensitivities. Table 2 summarizes the observations for the $z = 0.5 - 0.8$ sample, including the interferometer's configurations, the total integration time $t_{\rm int}$ over all configurations included for a given galaxy and the beam size. At this redshift, we observed the ^{12}CO(2-1) rotational transition (rest-frame frequency 230.538 GHz), shifted into the 2 mm band, with the interferometer in compact 'C' and 'D' configurations. Given the integration times, these configurations yield beam sizes comprised between $1'' - 5''$. Galaxies L14EG008, XA54 and XG55 were also observed in more extended configurations for higher resolution follow-ups, which will be presented in a future paper. The integration time per target was initially determined from the expected CO flux estimated from the SFR assuming a linear KS relation, requiring a signal-to-noise ratio (SNR) of at least 4, and later adapted in real time galaxy per galaxy during the observation campaign to ensure secure detections. One of the main goals of PHIBSS and PHIBSS2 is indeed to provide molecular gas estimates for a sample of star-forming galaxies covering different stellar masses and MS-offsets in an as unbiased way as possible.

Given the large number of observed hours, the weather conditions varied from excellent to very bad, with system temperatures ranging between 100 and 500 K depending on atmospheric conditions and season. We alternated source observations with bright quasar calibrators every 20 minutes to measure and remove the instrumental and atmospheric phase and amplitude fluctuations with time. The instrument response per frequency was further measured once per observational track on a strong quasar without spectral lines. The absolute flux scale was derived from secondary flux calibrators (MWC349 and LkHα101), whose fluxes are regularly measured using Jupiter satellites or planets. We mostly used receivers of temperature $T_{\rm rec} \sim 35 - 70$ K in band 2, but also the latest NOEMA receivers with better $T_{\rm rec} \sim 30 - 50$ K in the last 1.5 years. The observations were carried out using dual polarization in the Single Side Band mode and we used the Widex backend correlator with 3.6 GHz coverage per polarization. The source integration times lie around 7 hours to achieve similar signal-to-noise ratios under different weather conditions, except for the high-resolution follow-ups to be presented later, for which the integration times can reach about 30 hours. The data was calibrated using the CLIC package of the IRAM GILDAS software and further analyzed and mapped in its MAPPING environment. The spectra were analyzed with the CLASS package within GILDAS.

As for the PHIBBS survey and the data compilation used in Tacconi et al. (2018), the data from PHIBSS2 will be made publicly available at the end of the reduction and interpretation procedure at `http://www.iram.fr/~phibss2/Data_Release.html`.

3. Results

3.1. The PHIBSS2 sample at $z = 0.5 - 0.8$

The PHIBSS2 $z = 0.5 - 0.8$ sample of 61 near MS star-forming galaxies which is the focus of this article is presented in Table 1 and Fig. 1 & 2. Appendix A further presents HST I-band images of these galaxies, while section 3.4 presents their sizes and bulge-to-total (B/T) luminosity ratios. As can be seen in the HST I-band images and indicated in Table 1, the resulting sample comprises 49 disk-dominated and 12 bulge-dominated galaxies (80% and 20% of the sample,respectively), 36 of them having clear spiral or ring features (59%), highlighted in the residual maps. This repartition agrees very well with that found by Tacconi et al. (2013) for the PHIBSS sample and with larger HST imaging surveys (Wuyts et al. 2011b). A visual inspection also shows that 14 galaxies out of 61 (23%) harbor bars despite the intermediate redshift (Table 1). The relatively regular morphologies observed for most galaxies of the sample are compatible with them being isolated and not undergoing major mergers. Indeed, a visual inspection of the HST images indicates that only 4 galaxies out of 61 (7%) have both asymmetries and companions, which is comparable to the fraction of mergers from other MS studies (e.g., Tacconi et al. 2013; Wisnioski et al. 2015). Beyond the sample at $z = 0.5 - 0.8$ presented here, higher redshift PHIBSS2 samples at $z = 1 - 1.6$ and $z = 2 - 3$ will be presented in future articles.

3.2. CO fluxes

Tables 2 and 3 summarize the PHIBSS2 CO(2-1) line observations at $z = 0.5 - 0.8$. In Table 2, we indicate the interferometer's configuration, the total on-source observation time $t_{\rm int}$, the resulting CO beam size together with the redshift and position offsets of the detected CO emission (Δz, ΔR.A. and ΔDEC.), the peak CO luminosity $s_{\rm peak}$ from a Gaussian fit to the spatially-averaged spectrum, the associated root mean square (RMS) noise σ_{30} averaged over channels of 30 km.s^{-1} width, the full width half maximum (FWHM) from the Gaussian fit and its uncertainty dFWHM. In Table 3, we display the CO(2-1) line fluxes F(CO), which correspond to the mean value of three different estimates of the line intensity weighted by their respective uncertainties: (i) directly obtained from the spatially-integrated spectrum over the velocity window centered on the peak emission that maximizes the flux; (ii) derived from the Gaussian fit to the spatially-integrated spectrum, whose peak luminosity and FWHM are indicated in Table 2; and (iii) determined from the velocity-integrated line map (using the `GO FLUX` tool of `GILDAS`). The spatially-averaged spectra and the Gaussian fits are displayed in Appendix. A along with the HST I-band images. Amongst them, 8 galaxies clearly display double horned profiles which are characteristic of thin rotating disks. The flux uncertainty dF(CO) is estimated from the RMS noise integrated over the full line width, leading to the integrated flux signal-to-noise ratio SNR = F(CO)/dF(CO). The dispersion between the three estimates of the line intensity is in most cases well below the quoted uncertainty dF(CO). In the few cases where there were significant discrepancies between the three estimates, we selected the most reliable one. As shown in Table 3, we detected the CO(2-1) line emission in 60 of the 61 galaxies of the $z = 0.5 - 0.8$ sample, which corresponds to a detection rate of 97%. Amongst these detections, 5 have low SNR and display a slight offset from the HST I-band image or an ambiguous spatially-integrated spectrum: they are indicated as marginal in the table.

For the non-detected galaxy, we determine an upper limit from the experimental RMS noise as in Tacconi et al. (2018), i.e., corresponding to a flux that should have been detected at SNR > 3 with a 98% probability,

$$\mathrm{F}_{\rm upper} = (3 + 2.1) \times \sigma_{\rm F} \tag{1}$$

where $\sigma_{\rm F}$ is the RMS noise on the integrated line flux (e.g., Masci 2011). This latter quantity is evaluated as

$$\sigma_{\rm F} = \sigma_{30} \Delta V \sqrt{\frac{30\ \mathrm{km.s^{-1}}}{\Delta V}} = \sigma_{30} \sqrt{\Delta V \times 30\ \mathrm{km.s^{-1}}}, \tag{2}$$

where σ_{30} is the noise per 30 km.s^{-1} wide channel and ΔV the velocity width over which the signal is integrated when searching for the line.

3.3. Molecular gas masses

Although the CO molecule only represents a small fraction of the total molecular gas mass and its lower rotational lines are almost always optically thick, observations of giant molecular clouds (GMCs) in the Milky Way have shown that the integrated line flux of its rotational lines could be used as a quantitative tracer of the molecular gas mass (Dickman et al. 1986; Solomon et al. 1987; Combes 1991; Young & Scoville 1991; Solomon & Barrett 1991; Dame et al. 2001; Bolatto et al. 2013). The intrinsic CO luminosity associated to any region of flux can be expressed as

$$\left(\frac{\mathrm{L}'_{\rm CO}}{\mathrm{K.km.s^{-1}.pc^2}}\right) = \frac{3.25 \times 10^7}{1+z} \left(\frac{\mathrm{F(CO)}}{\mathrm{Jy.km.s^{-1}}}\right) \left(\frac{\nu_{\rm rest}}{\mathrm{GHz}}\right)^{-2} \left(\frac{\mathrm{D_L}}{\mathrm{Mpc}}\right)^2, \tag{3}$$

Table 1: The PHIBSS2 sample at $z = 0.5 - 0.8$

#	ID	Field	Source[a]	R.A. Optical	DEC. Optical	$z_{\rm optical}$	Morphology[b]	$M_\star$[c] ($M_\odot$)	SFR[d] ($M_\odot.yr^{-1}$)	sSFR[e] (Gyr^{-1})
1	XA53	COSMOS	822872	10:02:02.09	+02:09:37.40	0.7000	DC	2.9E+11	47.3	0.16
2	XC53	COSMOS	805007⋆	10:00:58.20	+01:45:59.00	0.6227	B	8.4E+10	47.1	0.56
3	XD53	COSMOS	822965	10:01:58.73	+02:15:34.20	0.7028	DSb	8.9E+10	39.5	0.44
4	XE53	COSMOS	811360	10:01:00.74	+01:49:53.00	0.5297	DSC	2.3E+10	25.5	1.13
5	XF53	COSMOS	834187	09:58:33.86	+02:19:50.90	0.5020	DSbA	1.2E+11	18.6	0.16
6	XG53	COSMOS	800405	10:02:16.78	+01:37:25.00	0.6223	DSAC	1.6E+11	21.0	0.13
7	XH53	COSMOS	837919	10:01:09.67	+02:30:00.70	0.7028	DSAC	5.4E+10	18.2	0.34
8	XI53	COSMOS	838956	10:00:24.70	+02:29:12.10	0.7026	B	2.9E+11	20.3	0.07
9	XL53	COSMOS	824759	10:00:28.27	+02:16:00.50	0.7506	BR	1.7E+11	28.6	0.17
10	XM53	COSMOS	810344	10:01:53.57	+01:54:14.80	0.7007	D	4.4E+11	23.9	0.05
11	XN53	COSMOS	839268	10:00:11.16	+02:35:41.60	0.6967	DSb	1.1E+11	24.2	0.22
12	XO53	COSMOS	828590	10:02:51.41	+02:18:49.70	0.6077	D	2.5E+11	11.7	0.05
13	XQ53	COSMOS	838696	10:00:35.69	+02:31:15.60	0.6793	DC	8.3E+10	26.9	0.32
14	XR53	COSMOS	816955	10:01:41.85	+02:07:09.80	0.5165	DSb	1.9E+11	14.5	0.08
15	XT53	COSMOS	823380	10:01:39.31	+02:17:25.80	0.7021	DSA	1.1E+11	22.7	0.20
16	XU53	COSMOS	831385	10:00:40.37	+02:23:23.60	0.5172	DSbA	1.9E+10	28.0	1.51
17	XV53	COSMOS	850140	10:01:43.66	+02:48:09.40	0.6248	DA	6.3E+10	23.1	0.36
18	XW53	COSMOS	824627⋆	10:00:35.52	+02:16:34.30	0.7503	DS	2.5E+10	13.7	0.54
19	L14CO001	COSMOS	831870	10:00:18.91	+02:18:10.10	0.5024	DSA	1.5E+10	29.0	1.87
20	L14CO004	COSMOS	831386	10:00:40.29	+02:20:32.60	0.6885	DC	2.8E+10	8.8	0.31
21	L14CO007	COSMOS	838945	10:00:25.18	+02:29:53.90	0.5015	DC	5.1E+10	4.1	0.08
22	L14CO008	COSMOS	820898	09:58:09.07	+02:05:29.76	0.6081	DSb	8.8E+10	13.9	0.16
23	L14CO009	COSMOS	826687	09:58:56.45	+02:08:06.72	0.6976	DS	2.8E+10	21.4	0.76
24	L14CO011	COSMOS	839183	10:00:14.30	+02:30:47.16	0.6985	DSbAC	2.6E+10	29.3	1.15
25	L14CO012	COSMOS	838449	10:00:45.53	+02:33:39.60	0.7007	B	3.9E+10	10.0	0.25
26	XA54	AEGIS	30084 (10098)	14:19:17.33	+52:50:35.30	0.6590	DS	1.3E+11	51.7	0.40
27	XB54	AEGIS	17329 (5038)	14:19:37.26	+52:51:03.40	0.6702	DS	1.7E+11	29.1	0.17
28	XC54	AEGIS	14885 (4097)	14:19:49.14	+52:52:35.80	0.5093	DSC	1.6E+11	37.9	0.24
29	XD54	AEGIS	24556 (8538)	14:19:46.35	+52:54:37.20	0.7541	DSA	2.3E+10	28.9	1.26
30	XE54	AEGIS	25608 (8310)	14:19:35.27	+52:52:49.90	0.5090	DS	2.5E+10	11.0	0.45
31	XF54	AEGIS	32878 (11378)	14:19:41.70	+52:55:41.30	0.7683	DS	5.1E+10	19.9	0.39
32	XG54	AEGIS	3654 (169)	14:20:13.43	+52:54:05.90	0.6593	DSbAC	1.4E+11	14.4	0.10
33	XH54	AEGIS	30516 (10745)	14:19:45.42	+52:55:51.00	0.7560	DSA	1.9E+10	13.1	0.70
34	L14EG006	AEGIS	23488 (7652)	14:18:45.52	+52:43:24.10	0.5010	DSbC	3.0E+10	7.4	0.25
35	L14EG008	AEGIS	21351 (7021)	14:19:39.46	+52:52:33.60	0.7315	DS	8.7E+10	79.5	0.91
36	L14EG009	AEGIS	31909 (11332)	14:20:04.88	+52:59:38.84	0.7359	DA	1.1E+10	9.9	0.89
37	L14EG010	AEGIS	4004 (725)	14:20:22.80	+52:55:56.28	0.6702	B	5.5E+10	9.3	0.17
38	L14EG011	AEGIS	6274	14:20:26.20	+52:57:04.85	0.5705	DSb	5.4E+10	25.7	0.48
39	L14EG012	AEGIS	6449 (515)	14:19:52.95	+52:51:11.06	0.5447	DSb	1.1E+11	9.1	0.08
40	L14EG014	AEGIS	9743	14:20:33.58	+52:59:17.46	0.7099	BC	8.5E+10	5.9	0.07
41	L14EG015	AEGIS	26964	14:20:45.61	+53:05:31.18	0.7369	B	9.3E+10	13.4	0.14
42	L14EG016	AEGIS	34302	14:18:28.90	+52:43:05.28	0.6445	DSb	4.0E+10	6.6	0.17
43	XA55	GOODS-N	21285 (9335)⋆	12:36:59.92	+62:14:50.00	0.7610	DSA	2.8E+10	44.7	1.58
44	XB55	GOODS-N	6666 (3091)†	12:36:08.13	+62:10:35.90	0.6790	B	4.5E+10	23.1	0.52
45	XC55	GOODS-N	19725 (8738)	12:36:09.76	+62:14:22.60	0.7800	DS	4.6E+10	29.1	0.64
46	XD55	GOODS-N	12097 (5385)	12:36:21.04	+62:12:08.50	0.7790	DRA	3.1E+10	21.6	0.70
47	XE55	GOODS-N	19815 (8798)⋆	12:36:11.26	+62:14:20.90	0.7720	D	3.3E+10	14.8	0.45
48	XF55	GOODS-N	7906 (3565)	12:35:55.43	+62:10:56.80	0.6382	DC	1.1E+10	11.1	0.96
49	XG55	GOODS-N	19257 (8697)	12:37:02.93	+62:14:23.60	0.5110	DSA	3.8E+10	8.5	0.22
50	XH55	GOODS-N	16987 (7668)	12:37:13.87	+62:13:35.00	0.7784	DS	1.6E+10	13.0	0.80
51	XL55	GOODS-N	10134 (4568)	12:37:10.56	+62:11:40.70	0.7880	DSC	3.2E+10	22.2	0.69
52	L14GN006	GOODS-N	30883 (12248)	12:36:34.41	+62:17:50.50	0.6825	DS	2.5E+10	23.8	0.95
53	L14GN007	GOODS-N	939 (334)	12:36:32.38	+62:07:34.10	0.5950	DS	7.4E+10	8.9	0.12
54	L14GN008	GOODS-N	11532 (5128)	12:36:07.83	+62:12:00.60	0.5035	DSb	1.9E+10	5.5	0.28
55	L14GN018	GOODS-N	25413 (10807)	12:36:31.66	+62:16:04.10	0.7837	DA	2.5E+10	32.8	1.31
56	L14GN021	GOODS-N	8738 (3875)	12:36:03.26	+62:11:10.98	0.6380	B	5.1E+10	76.9	1.50
57	L14GN022	GOODS-N	11460 (5127)⋆	12:36:36.76	+62:11:56.09	0.5561	B	1.3E+10	6.8	0.54
58	L14GN025	GOODS-N	36596 (14032)	12:37:13.99	+62:20:36.60	0.5320	BC	4.5E+10	3.5	0.08
59	L14GN032	GOODS-N	21683 (9558)	12:37:16.32	+62:15:12.30	0.5605	BC	1.3E+11	7.6	0.06
60	L14GN033	GOODS-N	1964 (918)	12:36:53.81	+62:08:27.70	0.5609	DSb	1.1E+10	6.7	0.59
61	L14GN034	GOODS-N	33895	12:36:19.68	+62:19:08.10	0.5200	DCA	7.4E+10	8.7	0.12

Notes.
[a] The source numbers correspond to the zCOSMOS nomenclature in the COSMOS field and to the 3D-HST v4.0 nomenclature in the other fields, with the 3D-HST v2.1 nomenclature indicated inside parentheses when applicable.
[b] Morphology derived by eye from the HST I-band images presented in Appendix A, with the following non-exclusive denominations: D for disk-dominated; B for bulge-dominated; S for spiral; Sb for barred spiral; R for ring; A for asymmetric or perturbed; C for the presence of companions.
[c] Stellar masses from SED fitting, assuming a Chabrier Initial Mass Function (IMF), with assumed systematic uncertainties of 0.2 dex.
[d] Extinction-corrected SFR_{UV+IR} from UV continuum measurements and IR 24 μm luminosities extrapolated with Herschel PACS calibrations to total infrared luminosities, with assumed systematic uncertainties of 0.2 dex.
[e] sSFR = SFR/$M_\star$.
⋆ Marginal detections.
† Non-detection.

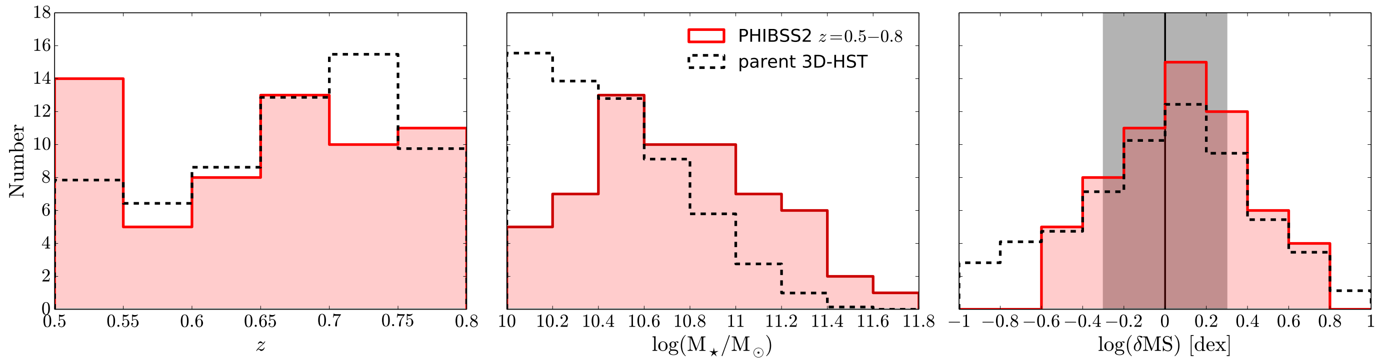

Fig. 2: Distribution of redshift (left panel), stellar mass (middle panel) and offset from the MS (right panel) for the PHIBSS2 $z = 0.5 - 0.8$ sample presented here, displayed in red. The offset from the MS is defined as $\delta\mathrm{MS} = \mathrm{sSFR}/\mathrm{sSFR_{MS}}(z, \mathrm{M_\star})$, where $\mathrm{sSFR_{MS}}(z, \mathrm{M_\star})$ is the analytical prescription for the center of the MS proposed in the compilation by Speagle et al. (2014). In the right panel, the solid black line indicates $\delta\mathrm{MS} = 1$ and the grey shaded area the ~0.3 dex scatter of the MS. While the PHIBSS2 $z = 0.5 - 0.8$ sample is highlighted in red, the dashed line corresponds to the parent 3D-HST distribution at $z = 0.5 - 0.8$ displayed in Fig. 1, with $10 < \log(\mathrm{M_\star/M_\odot}) < 11.8$ and $|\log(\delta\mathrm{MS})| < 1$ (i.e., within 1 dex of the MS line), normalized to match the same number of galaxies. The dip at low redshift is probably due to sky frequencies that made redshift determination more difficult or to cosmic variance. The mean and median stellar mass for the $z = 0.5 - 0.8$ subsample is $\log(\mathrm{M_\star/M_\odot}) = 10.7$.

Table 2: CO observations

#	ID	Field	Source	Config.	t_{int} (hr)	CO beam	Δz^a	ΔR.A.[b] (arcsec)	ΔDEC.[b] (arcsec)	$s_{\mathrm{peak}}{}^c$ (mJy)	$\sigma_{30}{}^d$ (mJy)	FWHM[e] (km.s^{-1})	dFWHM[e] (km.s^{-1})
1	XA53	COSMOS	822872	D	2.2	4.9″ × 3.9″	−0.0018	0.45	0.99	3.9	1.7	296	54.0
2	XC53	COSMOS	805007⋆	D	3.8	4.4″ × 3.4″	−0.0064	-0.90	-2.05	0.8	1.5	670	380.0
3	XD53	COSMOS	822965	D	4.3	4.2″ × 2.3″	−0.0008	-0.45	0.22	3.5	1.2	414	58.0
...	...	...	...	...	...	...	...	...	...	...	...	...	...

Only a small portion of the data is provided here. The full table will be available on the website `http://www.iram.fr/~phibss2/Data_Release.html`.

Notes.
[a] $\Delta z = z_{\mathrm{CO}} - z_{\mathrm{optical}}$, with z_{CO} from a Gaussian fit to the CO line. With typical redshift errors $\sigma_z = 0.003 \times (1 + z)$ (Momcheva et al. 2016), i.e., on average 0.005 in our sample at $z = 0.5 - 0.8$, all our detections except for XC53 and XE55 are within $\pm 0.4\sigma_z$.
[b] ΔR.A. = R.A.$_{\mathrm{CO}}$ − R.A.$_{\mathrm{optical}}$; ΔDEC. = DEC.$_{\mathrm{CO}}$ − DEC.$_{\mathrm{optical}}$.
[c] Peak CO luminosity from the Gaussian fit.
[d] Experimental RMS noise per 30 km.s^{-1} wide channel.
[e] FWHM from Gaussian fit and its uncertainty dFWHM.
⋆ Marginal detection.
† Non-detection.

Table 3: Integrated CO line flux and derived quantities

#	ID	Field	Source	F(CO)[a] (Jy.km.s^{-1})	dF(CO) (Jy.km.s^{-1})	SNR[b]	$\mathrm{L_{CO(2-1)}}{}^c$ (K.km.s^{-1}.pc^{-2})	$\mathrm{M_{gas}}{}^d$ (M$_\odot$)	μ^e_{gas}	$f_{\mathrm{gas}}{}^f$	$t_{\mathrm{depl}}{}^g$ (Gyr)
1	XA53	COSMOS	822872	1.45	0.46	3.2	9.4E+09	4.6E+10	0.16	0.14	1.0
2	XC53	COSMOS	805007⋆	0.20	0.08	2.5	1.0E+09	5.0E+09	0.06	0.06	0.1
3	XD53	COSMOS	822965	1.00	0.24	4.2	6.6E+09	3.3E+10	0.37	0.27	0.8
...	...	...	...	...	...	...	...	...	...	...	...

Only a small portion of the data is provided here. The full table will be available on the website `http://www.iram.fr/~phibss2/Data_Release.html`.

Notes.
[a] CO(2-1) integrated line flux.
[b] Signal-to-noise ratio SNR = F(CO)/dF(CO).
[c] Integrated CO(2-1) line luminosity as derived from Eq. 3.
[d] Molecular gas mass, corrected by a factor 1.36 for interstellar Helium, using a Galactic CO-H_2 conversion factor $\alpha_{\mathrm{CO}} = 4.36\ \mathrm{M_\odot/(K.km.s^{-1}.pc^2)}$ and a CO(2-1)/CO(1-0) line $r_{21} = 0.77$. The systematic uncertainties are evaluated at ±50%.
[e] $\mu_{\mathrm{gas}} = \mathrm{M_{gas}/M_\star}$.
[f] $f_{\mathrm{gas}} = \mathrm{M_{gas}/(M_{gas} + M_\star)} = \mu_{\mathrm{gas}}/(1 + \mu_{\mathrm{gas}})$.
[g] $t_{\mathrm{depl}} = \mathrm{M_{gas}/SFR}$.
⋆ Marginal detection.
† Non-detection.

where F(CO) is the velocity integrated flux, $\nu_{\rm rest}$ the rest-frame frequency – 230.538 GHz in the case of CO(2-1) –, and D_L the luminosity distance (Solomon et al. 1997). Considering a certain $J \rightarrow J-1$ CO line, the total molecular gas mass including a 36% correction to account for interstellar helium is then estimated as

$$M_{\rm gas} = \alpha_{\rm CO} L'_{\rm CO(J\rightarrow J-1)}/r_{J1} \tag{4}$$

where $\alpha_{\rm CO}$ is the CO(1-0) luminosity to moleculas gas mass conversion factor and $r_{J1} = L_{\rm CO(J\rightarrow J-1)}/L_{\rm CO(1-0)}$ the corresponding line ratio.

The $\alpha_{\rm CO}$ conversion factor a priori depends on the average cloud density, the Rayleigh-Jeans brightness temperature of the CO transition and the metallicity (Strong et al. 2004; Leroy et al. 2011; Genzel et al. 2012; Papadopoulos et al. 2012a; Bolatto et al. 2013; Sandstrom et al. 2013). In the Milky Way, its dense star-forming clumps, nearby MS star-forming galaxies and low metallicity galaxies, estimates of the conversion factor based on virial masses, optically thin tracers of the column density and diffuse gamma-ray emission stemming from the interaction between cosmic rays and interstellar medium protons seem to converge towards a relatively uniform value $\alpha_G = 4.36 \pm 0.9\ M_\odot/(\rm K.km.s^{-1}.pc^{-1})$ including helium (Strong & Mattox 1996; Dame et al. 2001; Grenier et al. 2005; Bolatto et al. 2008; Abdo et al. 2010; Schinnerer et al. 2010; Leroy et al. 2011; Bolatto et al. 2013). As the CO emission in the $z = 0.5{-}0.8$ galaxies studied in this paper is likely to originate from virialized GMCs with mean densities of the same order of magnitude as their lower redshift counterparts (Daddi et al. 2008, 2010a; Dannerbauer et al. 2009) and similar dust temperatures (Magnelli et al. 2009; Hwang et al. 2010; Elbaz et al. 2011), their conversion factor should be relatively close to the 'Galactic' conversion factor α_G. But since the CO conversion factor increases with decreasing metallicity as the CO molecule gets more photo-dissociated (Wolfire et al. 2010; Bolatto et al. 2013), we do account for its metallicity dependence. From the different metallicity corrections proposed in the literature, we adopt the geometric mean of the recipes by Bolatto et al. (2013) and Genzel et al. (2012) as adopted by Genzel et al. (2015) and Tacconi et al. (2018):

$$\alpha_{\rm CO} = \alpha_G \sqrt{0.67 \times \exp(0.36 \times 10^{8.67-\log Z}) \times 10^{-1.27\times(\log Z - 8.67)}} \tag{5}$$

where $\log Z = 12 + \log(\rm O/H)$ is the metallicity on the Pettini & Pagel (2004) scale estimated from the mass-metallicity relation

$$\log Z = 8.74 - 0.087 \times (\log(M_\star) - b)^2 \tag{6}$$

with $b = 10.4 + 4.46 \times \log(1 + z) - 1.78 \times (\log(1 + z))^2$ (Genzel et al. 2015, and references therein). This metallicity correction leads to a mean $\alpha_{\rm CO} = 4.0 \pm 0.3\ M_\odot/(\rm K.km.s^{-1}.pc^{-1})$ within the $z = 0.5 - 0.8$ sample.

The r_{21} line ratio converts the observed CO(2-1) luminosity into the CO(1-0) luminosity for which the $\alpha_{\rm CO}$ conversion factor is calibrated. While a thermally excited transition in the Rayleigh-Jeans domain with $r_{21} = 1$ has often been assumed to derive molecular gas masses (Combes et al. 2011, 2013; Bauermeister et al. 2013; Tacconi et al. 2013), the CO(2-1) line could both be sub-thermally excited and require a Planck-correction, leading to $r_{21} < 1$. In particular, Leroy et al. (2009) obtain values of r_{21} between 0.6 and 1 within a sample of 18 nearby galaxies, with a typical value $r_{21} \sim 0.8$, while Dannerbauer et al. (2009) and Aravena et al. (2010) obtain $r_{21} \sim 0.85$ at $z \sim 1.5$, and Papadopoulos et al. (2012b) around $r_{21} = 0.91$ for a large sample of luminous and ultra-luminous infrared galaxies in the local Universe. Bothwell et al. (2013) further measure $r_{21} \sim 0.84$ within a sample of 40 luminous sub-millimiter galaxies between $z = 1 - 4$ while Daddi et al. (2015) find an average $r_{21} = 0.76$ from a sample of 4 galaxies at $z = 1.5$. In the following we assume $r_{21} = 0.77$, as also assumed by Genzel et al. (2015) and Tacconi et al. (2018).

The resulting values of the intrinsic CO(2-1) luminosity $L_{\rm CO(2-1)}$ and the molecular gas mass $M_{\rm gas}$ as well as the corresponding gas to stellar mass ratio $\mu_{\rm gas} = M_{\rm gas}/M_\star$, gas fraction $f_{\rm gas} = M_{\rm gas}/(M_{\rm gas} + M_\star) = \mu_{\rm gas}/(1 + \mu_{\rm gas})$ and depletion time $t_{\rm depl} = M_{\rm gas}/\rm SFR$ are diplayed in Table 3. The relative uncertainty on the CO(2-1) line flux dF(CO)/F(CO) = 1/SNR is 30% on average and up to about 50%, which is transferred to the intrinsic CO luminosity $L_{\rm CO(2-1)}$. Considering the 30% uncertainty on the Galactic conversion factor α_G (Bolatto et al. 2013), the sytematic difference up to 20% between the metallicity corrections of Bolatto et al. (2013) and Genzel et al. (2012) in the metallicity range of the $z = 0.5 - 0.8$ sample that reflects the scatter in the $\alpha_{\rm CO}$-metallicity relation and the more negligible 12% uncertainty on the r_{21} line ratio from Daddi et al. (2015) leads to a systematic uncertainty of at least 50% on the final molecular gas masses. Fig. 3 shows the distributions of $\mu_{\rm gas}$, $f_{\rm gas}$ and $t_{\rm depl}$, comparing them with those obtained at $z = 0$ from the COLDGASS survey (Saintonge et al. 2011a,b) and at $z = 1 - 2$ with the first PHIBSS program (Tacconi et al. 2010, 2013). The gas-to-stellar mass ratios $\mu_{\rm gas}$ range from 0.03, close to the detection limit, to 1.8, with a median $\widetilde{\mu_{\rm gas}} = 0.28 \pm 0.04$. The ranges for $f_{\rm gas}$ and $t_{\rm depl}$ are respectively $0.03 - 0.64$ and $0.11 - 3.82$ Gyr, with median values $\widetilde{f_{\rm gas}} = 0.22 \pm 0.02$ and $\widetilde{t_{\rm depl}} = 0.84 \pm 0.07$ Gyr. These values are intermediary between their low- and high-redshift counterparts, fitting well with a significantly increasing gas fraction and a slightly decreasing depletion time with redshift. In fact, they are in excellent agreement with the values expected from the scaling relations obtained by Tacconi et al. (2018) within their comprehensive sample of about 1400 CO and dust molecular gas measurements between $z = 0$ and $z = 4.6$. Indeed, applying the scaling relations on the MS (δMS = 0) at the median redshift $z = 0.67$ and $\log(M_\star/M_\odot) = 10.7$ of the sample yields 0.27, 0.21 and 0.90 for the gas-to-stellar mass ratio, the gas fraction and the depletion time. Since the molecular gas content of galaxies increases strongly with redshift (Daddi et al. 2010b; Tacconi et al. 2010, 2013, 2018; Genzel et al. 2015; Lagos et al. 2015) while their atomic gas content varies much slower (e.g., Bauermeister et al. 2010) with three times more HI mass at $z = 0$ (Saintonge et al. 2011a), molecular gas is expected to dominate above $z \sim 0.4$ and in particular in our $z = 0.5 - 0.8$ sample. The molecular gas to stellar ratio $\mu_{\rm gas}$ and gas fraction $f_{\rm gas}$ thus approximately probe the total gas fractions.

Noting from Figs. 1 and 2 that the mass distribution of the PHIBSS2 $z = 0.5 - 0.8$ sample differ from its CANDELS/3D-HST parent distribution, we further derive mass-matched median values for the molecular gas-to-stellar mass ratio, gas fraction and depletion time. Following Catinella et al. (2010) and Saintonge et al. (2011a), we place galaxies in stellar mass bins of 0.2 dex width as in the central panel of Fig. 2 and assign as weight the ratio between the number of galaxies in the CANDELS/3D-HST parent sample within 1 dex of the MS line and that in the PHIBSS2 sample at $z = 0.5 - 0.8$ in each of these stellar mass bins. Limiting ourselves to stellar masses above $\log(M_\star/M_\odot) \geq 10.4$ to avoid being affected by the sparsely populated bins below this value, the resulting mass-weighted medians are $\overline{\mu_{\rm gas}} =$

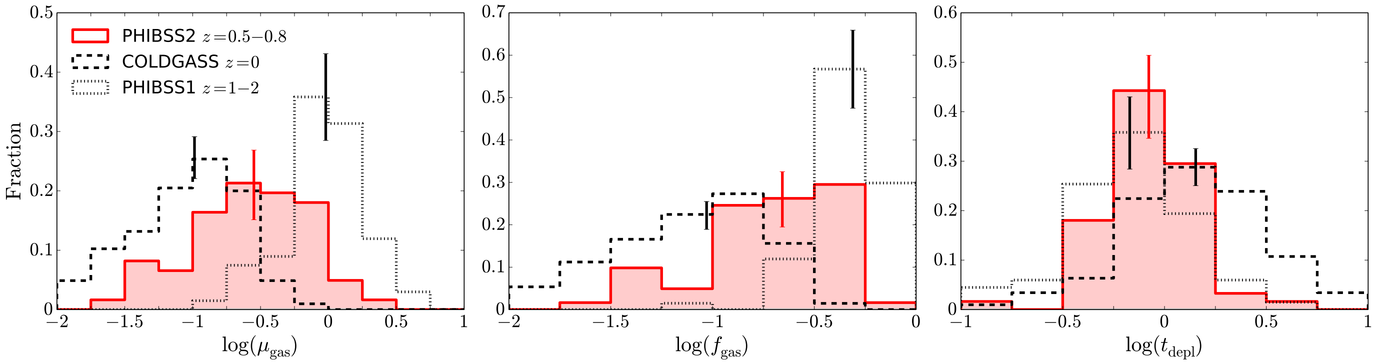

Fig. 3: Distributions of the molecular gas to stellar mass ratio μ_{gas}, gas fraction f_{gas} and of depletion time t_{depl} for the PHIBSS2 $z = 0.5 - 0.8$ sample, whose medians are $\widetilde{\mu_{\mathrm{gas}}} = 0.28 \pm 0.04$, $\widetilde{f_{\mathrm{gas}}} = 0.22 \pm 0.02$ and $\widetilde{t_{\mathrm{depl}}} = 0.84 \pm 0.07$ Gyr with respective dispersions of 0.42, 0.33 and 0.23 dex. The corresponding distributions of the total, non mass-matched $z \sim 0$ COLDGASS survey (dashed lines; Saintonge et al. 2011a,b) and of the $z = 1.2-2.2$ PHIBSS survey (dotted lines; Tacconi et al. 2010, 2013) are indicated for comparison. The medians are respectively 0.10, 0.09 and 1.42 Gyr for the COLDGASS survey and 0.96, 0.49 and 0.67 Gyr for the PHIBSS survey. Typical Poisson errors are shown at the positions of the medians for the different surveys.

0.30 ± 0.04, $\overline{f_{\mathrm{gas}}} = 0.23 \pm 0.02$ and $\overline{t_{\mathrm{depl}}} = 0.84 \pm 0.08$Gyr, which correspond well to the values expected from Tacconi et al. (2018) at the median stellar mass and redshift of the CANDELS/3D-HST parent sample with $10.4 < \log(\mathrm{M}_\star/\mathrm{M}_\odot) < 11.8$ and $|\log(\delta\mathrm{MS})| < 1$ (respectively, 0.29, 0.22 and 0.89). However, we leave the detailed study of the influence of mass selection on the Tacconi et al. (2018) scaling relations and in particular on their zero points to future works.

3.4. Size and morphology

The radial distribution of the star-forming molecular gas in most nearby galaxies follows an exponential profile reminiscent of the stellar disk (e.g., Young & Scoville 1982; Scoville & Young 1983; Young 2000) while bulges are mostly made of old stars (e.g., Wyse et al. 1997; Zoccali et al. 2003; Freeman 2008). To address the influence of morphology on star formation and to separate the contribution of disk and bulge, we not only determine the total half-light radius of the galaxies of the PHIBSS2 $z = 0.5 - 0.8$ sample from single Sérsic fits but also decompose them as two-component bulge disk systems with the 2D morphology fitting code `galfit` (Peng et al. 2002, 2010a). The fits are carried out on publicly available high resolution (0.03 arcsec per pixel) HST Advanced Camera for Survey (ACS) images in the F814W I-band. This band is optimal for our study as it is available for all the galaxies of the sample and probes the blue young stellar population at $z = 0.5 - 0.8$ while avoiding the rest-frame UV light from very young stars. The disk is described by an exponential profile (Freeman 1970)

$$I(R) = I_{\mathrm{d}} e^{-R/R_{\mathrm{e}}}, \tag{7}$$

where I_{d} is the disk central density and R_{e} its scale length, which is proportional to the disk half light radius $R_{\mathrm{d}} = 1.67835 R_{\mathrm{e}}$. The bulge is described by a Sersic (1968) profile

$$I(R) = I_{\mathrm{b}} e^{-b_n (R/R_{\mathrm{b}})^{1/n}} \tag{8}$$

assuming a classic de Vaucouleurs Sérsic index $n = 4$ as in Bruce et al. (2012), Lang et al. (2014) and Contini et al. (2016), I_{b} being the bulge central density and R_{b} its half-light radius. The parameter b_n depends on the Sérsic index n and is derived from $\Gamma(2n) = 2\gamma(2n, b_n)$, where Γ is the gamma function and γ the lower incomplete gamma function The centers of both components are left free but within 2 pixels of each other and their position angles constrained to be equal. We impose the bulge to be as or less elongated than the disk. Following Lang et al. (2014), we also consider pure disk and pure $n = 4$ bulge models. The `galfit` fits are carried out with a point spread function (PSF) obtained by averaging the 3D-HST (Skelton et al. 2014; Momcheva et al. 2016) PSF in the three fields of interest (AEGIS, COSMOS and GOODS-N) and a uniform weight map motivated by the nearly uniform HST weight maps around the $z = 0.5-0.8$ sources but which does not account for potential Poisson errors in the high flux regions. We refer to Häussler et al. (2007), Bruce et al. (2012), Lang et al. (2014) and Contini et al. (2016) for the influence of the PSF, the weight map and the background subtraction on `galfit` models. Neighboring nearby galaxies or satellites are fitted simultaneously with a single Sérsic model to account for their luminosity distribution.

One of the main difficulty when carrying multi-component fits with `galfit` is to avoid being trapped in a local χ^2 minimum depending on the initial guess instead of the global minimum (e.g., Häussler et al. 2007; Peng et al. 2010a; Bruce et al. 2012). Following Lang et al. (2014), we first build 10 initial guesses from the less degenerate single Sérsic fits using an empirical analysis of noise-free two-component models: (i) we generate a grid of ideal, noise-free two-component bulge disk models with different B/T and $\mathrm{R_b/R_d}$; (ii) we obtain their global Sérsic indices and half-light radii with `galfit` using no PSF and a weight map corresponding to ideal Poisson noise; (iii) we estimate the B/T associated to a series of 10 values of $\mathrm{R_b/R_d}$ for each galaxy from its Sérsic index using the result of the previous step; and (iv) we determine the corresponding bulge and disk to be used in the 10 initial guesses for that galaxy. Noting that not all single Sérsic fits yield physical half-light radii, we also build initial guesses from the pure bulge and pure disk fits with different values of B/T and $\mathrm{R_b/R_d}$ (10 values of $\mathrm{R_b/R_d}$ between 0.1 and 1, B/T = 0.1 and 0.5 when using the pure disk model, B/T = 0.5 and 0.9 when using the pure bulge model), leading to a total of 52 `galfit` runs per galaxy for the bulge disk model, including the pure bulge and pure disk models. The best-fit model is that with the lower reduced χ^2, casting away models where the bulge is implausibly small ($R_{\mathrm{b}} < 0.1$ pixel) or larger than the disk ($R_{\mathrm{b}} > R_{\mathrm{d}}$), except for L14GN025 (`GN4-36596`) where we

Table 4: I-band morphology and sizes

#	ID	Field	Source	$R_{\rm Sersic}{}^{a}$ (kpc)	$n^{a}_{\rm Sersic}$	$q^{a}_{\rm Sersic}$	$R_{\rm d}{}^{b}$ (kpc)	$R_{\rm b}{}^{b}$ (kpc)	B/T^{c}
1	XA53	COSMOS	822872	7.70	2.17	0.62	6.82	6.65	0.45
2	XC53	COSMOS	805007*	2.71	4.00	0.77	3.50	1.24	0.61
3	XD53	COSMOS	822965	7.20	1.53	0.92	10.13	2.34	0.16
4	XE53	COSMOS	811360	5.35	1.02^{+}	0.83	5.61	0.46	0.02
5	XF53	COSMOS	834187	15.37	4.00	0.57	8.59	4.36	0.37
6	XG53	COSMOS	800405	4.21	3.86^{+}	0.82	-	4.49	1.00
7	XH53	COSMOS	837919	4.36	3.34	0.79	3.58	3.51	0.70
8	XI53	COSMOS	838956	4.66	3.10^{+}	0.77	-	7.30	1.00
9	XL53	COSMOS	824759	2.76	2.95^{+}	0.73	-	4.35	1.00
10	XM53	COSMOS	810344	4.81	1.86	0.43	4.44	3.85	0.29
11	XN53	COSMOS	839268	7.02	4.00	0.79	-	6.42	1.00
12	XO53	COSMOS	828590	3.31	2.32^{+}	0.51	5.66	5.21	0.81
13	XQ53	COSMOS	838696	32.42	4.00	0.45	16.41	7.75	0.38
14	XR53	COSMOS	816955	18.95	4.00	0.73	15.75	4.78	0.30
15	XT53	COSMOS	823380	7.21	2.73^{+}	0.66	6.07	5.93	0.54
16	XU53	COSMOS	831385	5.84	0.90	0.47	6.36	0.61	0.02
17	XV53	COSMOS	850140	3.93	1.19	0.41	4.42	2.04	0.13
18	XW53	COSMOS	824627*	4.61	1.19	0.86	4.55	0.34	0.02
19	L14CO001	COSMOS	831870	2.84	1.20	0.92	2.97	0.47	0.03
20	L14CO004	COSMOS	831386	3.51	1.53	0.54	3.66	2.06	0.19
21	L14CO007	COSMOS	838945	15.13	3.37	0.39	10.30	7.55	0.52
22	L14CO008	COSMOS	820898	7.05	2.17	0.62	6.08	4.46	0.29
23	L14CO009	COSMOS	826687	7.28	1.24^{+}	0.56	6.53	-	0.00
24	L14CO011	COSMOS	839183	6.16	0.59	0.71	8.00	0.93	0.03
25	L14CO012	COSMOS	838449	1.71	1.74	0.83	1.73	1.72	0.39
26	XA54	AEGIS	30084	9.80	2.17	0.89	6.56	0.64	0.05
27	XB54	AEGIS	17329	20.54	4.00	0.97	18.15	1.79	0.10
28	XC54	AEGIS	14885	12.76	0.32^{+}	0.17	17.47	0.53	0.01
29	XD54	AEGIS	24556	3.75	0.54^{+}	0.81	4.62	-	0.00
30	XE54	AEGIS	25608	8.30	0.29^{+}	0.26	9.72	-	0.00
31	XF54	AEGIS	32878	9.92	2.19	0.72	7.15	1.86	0.10
32	XG54	AEGIS	3654	38.20	4.00^{+}	0.57	13.47	3.38	0.17
33	XH54	AEGIS	30516	4.95	0.78	0.78	5.74	0.27	0.02
34	L14EG006	AEGIS	23488	9.85	1.84	0.60	8.20	2.81	0.09
35	L14EG008	AEGIS	21351	21.89	4.00	0.70	8.38	0.88	0.09
36	L14EG009	AEGIS	31909	2.81	0.46^{+}	0.78	3.42	-	0.00
37	L14EG010	AEGIS	4004	1.77	2.84^{+}	0.85	-	2.80	1.00
38	L14EG011	AEGIS	6274	11.57	1.86	0.57	9.23	2.76	0.07
39	L14EG012	AEGIS	6449	13.49	4.00	0.61	10.53	3.23	0.37
40	L14EG014	AEGIS	9743	3.92	1.68^{+}	0.93	3.21	2.72	0.14
41	L14EG015	AEGIS	26964	2.10	2.60^{+}	0.82	-	3.80	1.00
42	L14EG016	AEGIS	34302	4.61	2.23	0.77	3.74	3.72	0.36
43	XA55	GOODS-N	21285*	3.84	0.33^{+}	0.62	5.54	-	0.00
44	XB55	GOODS-N	6666†	1.69	2.60^{+}	0.87	-	2.85	1.00
45	XC55	GOODS-N	19725	3.11	3.00^{+}	0.98	3.77	3.16	0.77
46	XD55	GOODS-N	12097	2.55	0.35^{+}	0.59	3.55	-	0.00
47	XE55	GOODS-N	19815*	6.16	0.85	0.22	7.10	0.57	0.04
48	XF55	GOODS-N	7906	7.16	0.54^{+}	0.17	8.43	-	0.00
49	XG55	GOODS-N	19257	4.32	2.71^{+}	0.76	3.80	3.78	0.61
50	XH55	GOODS-N	16987	5.59	0.48^{+}	0.78	7.18	0.45	0.01
51	XL55	GOODS-N	10134	9.46	1.53	0.66	8.19	1.52	0.04
52	L14GN006	GOODS-N	30883	4.51	1.08	0.29	4.94	4.71	0.15
53	L14GN007	GOODS-N	939	6.55	3.03^{+}	0.69	-	11.43	1.00
54	L14GN008	GOODS-N	11532	8.38	1.86	0.85	6.57	0.73	0.04
55	L14GN018	GOODS-N	25413	3.51	1.00	0.81	3.75	0.11	0.01
56	L14GN021	GOODS-N	8738	0.93	2.14	0.91	1.31	1.07	0.71
57	L14GN022	GOODS-N	11460*	0.91	1.63	0.96	0.88	0.86	0.27
58	L14GN025	GOODS-N	36596	0.97	1.72	0.52	0.67	5.44	0.64
59	L14GN032	GOODS-N	21683	2.32	2.79^{+}	0.89	-	4.10	1.00
60	L14GN033	GOODS-N	1964	13.50	4.00	0.96	8.21	0.91	0.12
61	L14GN034	GOODS-N	33895	8.34	1.28	0.44	8.48	1.37	0.04

Notes.
[a] Half-light radius, Sérsic index and axis ratio of the single Sérsic fits in the F814W I-band images. Sérsic indices followed by a cross (+) correspond to cases where the single-Sérsic fit is better than the two-component fit (39% of the sample).
[b] Half-light radii of the $n = 1$ disk and $n = 4$ bulge components of the two-component fits in the I-band images.
[c] Bulge-to-total luminosity ratios defined from the two-component fits using Eq. 9.
* Marginal detection;
† Non-detection.

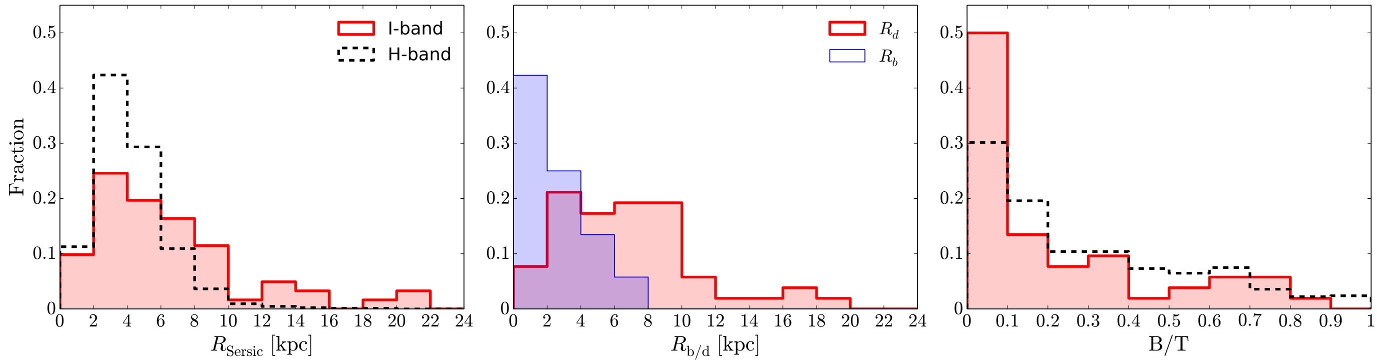

Fig. 4: Distributions of the single-Sérsic, disk and bulge half light radii together with the bulge-to-total luminosity ratio of the PHIBSS2 $z = 0.5 - 0.8$ sample determined with `galfit` from their HST/ACS I-band images. In the middle and right panels, we only consider galaxies with $B/T \neq 1$. The black dashed lines correspond to the corresponding parent CANDELS/3D-HST H-band distributions at $z = 0.5 - 0.8$ with $10 < \log(M_\star/M_\odot) < 11.8$ and $|\log(\delta MS)| < 1$ (van der Wel et al. 2012; Lang et al. 2014).

release this latter condition as the low surface brightness of the stellar halo in which the disk is embedded makes all models with $R_b < R_d$ unsatisfactory. We note that as in Lang et al. (2014), two-component decompositions are preferred over single Sérsic fits for about 2/3 of the sample, namely for 37 galaxies out of 61 (61%). The best-fit models are displayed with the I-band images in Appendix A.

Table 4 displays the results of both the single Sérsic and the two-component fits, with the half-light radius $R_{\rm Sersic}$, Sérsic index $n_{\rm Sersic}$, axis ratio $q_{\rm Sersic}$ resulting from the single Sérsic fits, the disk and bulge half-light radii R_d and R_b of the two-component fits as well as the corresponding bulge-to-total luminosity ratio B/T for the PHIBSS2 sample at $z = 0.5 - 0.8$. The Sérsic index $n_{\rm Sersic}$ is constrained to be between 0.2 and 4, and we note that $n_{\rm Sersic} = 4$ often coincides with relatively large values of the half-light radius $R_{\rm Sersic}$ that are usually corrected with the two-component fits. The bulge-to-total luminosity ratio is estimated from the two-component model as

$$B/T = \frac{F_b}{F_b + F_d} = \frac{1}{1 + 10^{(m_b - m_d)/2.5}}, \tag{9}$$

where F_b and F_d are respectively the total fluxes associated to the bulge and disk components, and m_b, m_d the associated magnitudes. Assuming that the uncertainties on the single-Sérsic fit parameters only depend on the signal-to-noise ratio, we transpose the results of van der Wel et al. (2012) to band I and conservatively evaluate the uncertainties on $R_{\rm Sersic}$, $n_{\rm Sersic}$ and $q_{\rm Sersic}$ at about 20% given the magnitude of the sources. We note that Bruce et al. (2012) find that the background subtraction induces errors of about 5% for $n_{\rm Sersic}$ and 10% for $R_{\rm Sersic}$, to which we should add the uncertainties introduced by the PSF choice and those intrinsic to `galfit` such as the choice of the weight matrix. From Lang et al. (2014), we infer a 0.05 uncertainty on B/T. Fig. 4 shows the distributions of the I-band $R_{\rm Sersic}$, R_d, R_b and B/T within the sample. The parent CANDELS/3D-HST measurements in the H-band (van der Wel et al. 2012; Lang et al. 2014) are shown for comparison in the case of $R_{\rm Sersic}$ and B/T. As most $B/T = 1$ cases correspond to galaxies harboring clear spiral features that are not well accounted by the cylindrically symmetric models adopted here, we do not show them in the middle and right panels. More generally, asymmetries and structures such as spiral arms, rings and bars may introduce biases in the B/T measurements. Accounting for such features would require a case-by-case study that is beyond the scope of this article, in which we favor a systematic approach to the determination of B/T compatible with large datasets, in line with other surveys (e.g., van der Wel et al. 2012; Lang et al. 2014; Contini et al. 2016). Compared to the H-band measurements, the I-band half-light radii are more spread out with a higher median value while half of the sample are found to be disks with very faint or non-existent bulges ($B/T < 0.1$). These trends relate to the lower characteristic wavelength of the I-band, which traces younger stars and hence highlight the disk relatively to the H-band images.

4. Discussion

4.1. Molecular gas fraction and depletion time

The PHIBSS2 legacy program provides an unprecedently large sample of CO molecular gas measurements at intermediate redshift with its 60 CO(2-1) detections between $z = 0.5 - 0.8$. As shown in section 3.3, the median molecular gas masses, gas-to-stellar mass ratios, gas fractions and depletion times obtained for the PHIBSS2 $z = 0.5 - 0.8$ sample are in excellent agreement with the scaling relations established by Genzel et al. (2015) and Tacconi et al. (2018) on a much larger sample of about 1400 sources between $z = 0 - 4.5$ including both CO and dust observations. These relations, which characterize the dependence of the molecular gas-to-stellar mass ratio and the depletion time on redshift, stellar mass, MS-offset and galaxy size, constitute the main contribution of the PHIBSS2 program to understand star formation processes on the MS across cosmic time. The molecular gas-to-stellar mass ratio $\mu_{\rm gas}$ and the depletion time $t_{\rm depl}$ are written as power law functions of redshift, stellar mass, distance from the MS and galaxy size such that their logarithms yield

$$\log(y) = A + B\log(1+z) + C\log(\delta MS) + D\log(\delta M) + E\log(\delta R), \tag{10}$$

where A, B, C and D are constants determined from the observations, $\delta MS = sSFR/sSFR(MS, z, M_\star)$ with $sSFR(MS, z, M_\star)$ the mean sSFR on the MS, $\delta M = M_\star/5.10^{10} M_\odot$ and $\delta R = R_{\rm Sersic}/R(MS, z, M_\star)$ with $R(MS, z, M_\star)$ the mean half-light radius on the MS, for example from van der Wel et al. (2014): $R(MS, z, M_\star) = 8.9\times(1+z)^{-0.75}(M_\star/M_\odot)^{0.23}$ kpc. In particular, while part of the scatter of the MS is due to the stochasticity of the cosmic accretion, the galaxies' individual histories and

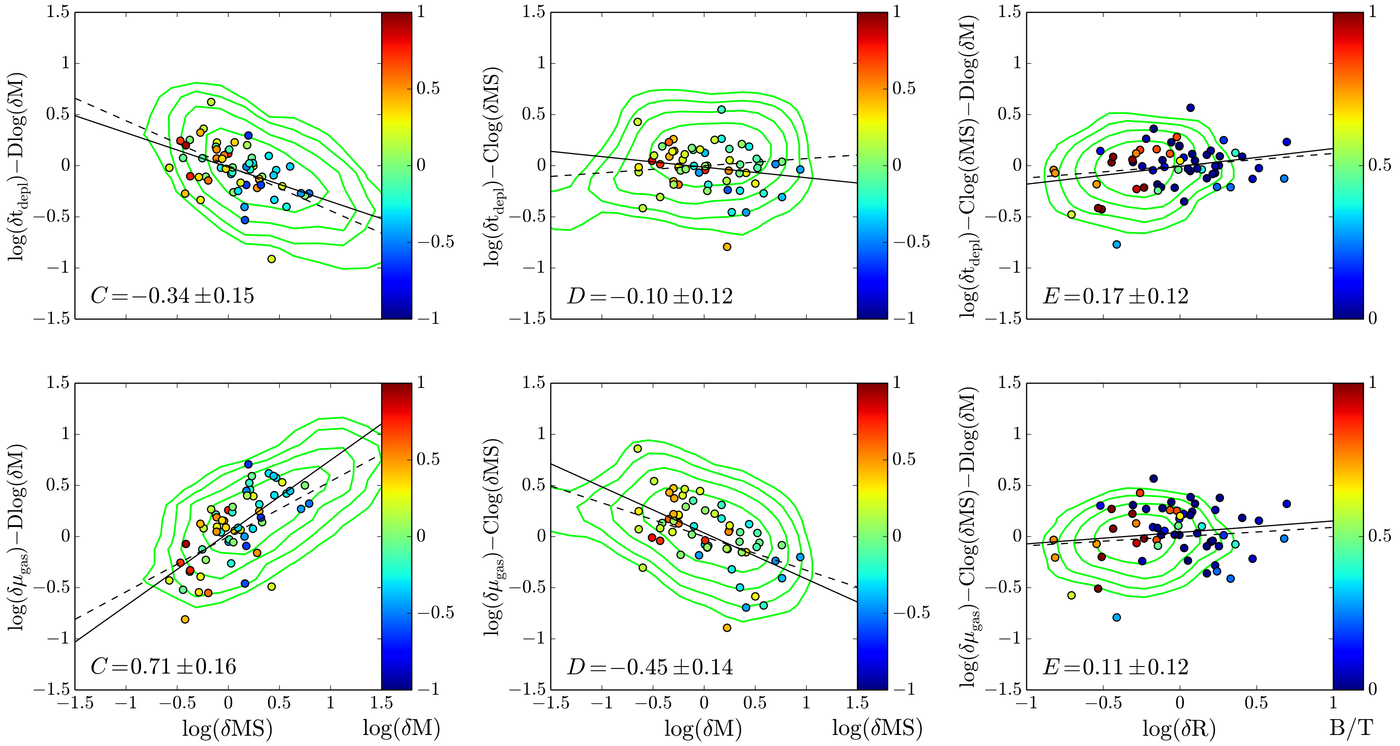

Fig. 5: Dependence of the residual molecular depletion time and gas to stellar mass ratio after subtraction of the redshift dependence on the distance from the MS, stellar mass and disk size within the PHIBSS2 $z = 0.5 - 0.8$ sample, compared to the dependencies deriving from the scaling relations obtained by Tacconi et al. (2018). We assume that the different variables can be separated as in Eq. 10 and 11, and plot each dependency independently. The black solid lines and the values indicated on the plots refer to the best fits for the $z = 0.5 - 0.8$ subsample, while the green contours and the dashed lines correspond to the comprehensive dataset studied by Tacconi et al. (2018) and its fitting formulae ($C = -0.44 \pm 0.04$, $D = +0.07 \pm 0.05$ and $E = +0.12 \pm 0.12$ for $t_{\rm depl}$ and $C = +0.54 \pm 0.03$, $D = -0.32 \pm 0.03$ and $E = +0.09 \pm 0.09$ for $\mu_{\rm gas}$).

their environment, morphology and fundamental physical quantities of star-forming galaxies such as their molecular gas fraction and depletion time vary progressively with δMS. This variation was already highlighed in different studies (e.g., Schiminovich et al. 2007; Wuyts et al. 2011b; Saintonge et al. 2011b, 2012; Magdis et al. 2012a; Huang & Kauffmann 2014; Genzel et al. 2015; Tacchella et al. 2016a), but Genzel et al. (2015) and Tacconi et al. (2018) quantify it precisely through the coefficient C. Tacconi et al. (2018) further add a non linearity in the redshift evolution of the molecular gas fraction to follow more closely the observations, namely considering a redshift evolution of the form $B\,(\log(1+z) - F)^{\beta}$ instead of the linear trend of Eq. 10, where F and β are additional constants. We define the residual

$$\log(\delta y) = \log(y) - A - B \times (\log(1+z) - F)^{\beta} \qquad (11)$$

when the redshift dependence is subtracted from the original quantity $\log(y)$. We determine $\delta t_{\rm depl}$ and $\delta\mu_{\rm gas}$ for the galaxies of the PHIBSS2 $z = 0.5 - 0.8$ sample, subtracting the redshift dependence obtained by Tacconi et al. (2018), and study their dependence on δMS, δM and δR. As can be seen in Fig. 5, these dependencies are in good agreement with the scaling relations of Tacconi et al. (2018), although with much bigger uncertainties due to our more limited sample. Coefficients C and D were obtained through simultaneous linear fits of the redshift-subtracted quantities $\log(\delta y)$ as a function of $\log(\delta$MS$)$ and $\log(\delta$M$)$ while E results from a single linear fit of the residual $(\log(\delta y) - \mathrm{C}\log(\delta \mathrm{MS}) - \mathrm{D}\log(\delta \mathrm{M}))$ as a function of $\log(\delta$R$)$. The uncertainties are evaluated by assuming a 0.3 dex uncertainty on $\mu_{\rm gas}$ and $t_{\rm depl}$ and 0.2 dex uncertainties on δMS, δM and δR. This illustrates Appendix A of Tacconi et al. (2018), which shows from model data sets driven by the actual data that the MS-offset and stellar mass dependencies of the molecular gas-to-stellar mass ratio and depletion time can be recovered from data sets with $N \gtrsim 40$ sources as long as the coverage in δMS and δM exceeds 1 dex – which is the case here.

4.2. Kennicutt-Schmidt relation

In Fig. 6, we plot the KS relation between SFR and molecular gas mass surface densities $\Sigma_{\rm SFR} = 0.5\ {\rm SFR}/\pi R^2_{\rm Sersic}$ and $\Sigma_{\rm gas} = 0.5\ {\rm M_{gas}}/\pi R^2_{\rm Sersic}$ within the $z = 0.5 - 0.8$ PHIBSS2 sample. A linear least square fit to the data yields a KS exponent $N = 1.02 \pm 0.08$ assuming 0.3 dex uncertainties in both SFR and molecular gas surface densities. This strikingly linear relation with Pearson correlation coefficient $r = 0.94$ corresponds to a uniform depletion time $t_{\rm depl} = 0.82$ Gyr in line with the Tacconi et al. (2018) scaling relations, the residual scatter being 0.24 dex. We also tested definitions of $\Sigma_{\rm SFR}$ and $\Sigma_{\rm gas}$ using the disk radius $R_{\rm d}$ instead of $R_{\rm Sersic}$, yielding similar results. The main contributor to the 0.24 dex scatter may be the different evolutionary stages of the molecular clouds within galaxies and their dynamical environment (e.g., Lada et al. 2010; Lombardi et al. 2010; Onodera et al. 2010; Schruba et al. 2010; Murray et al.

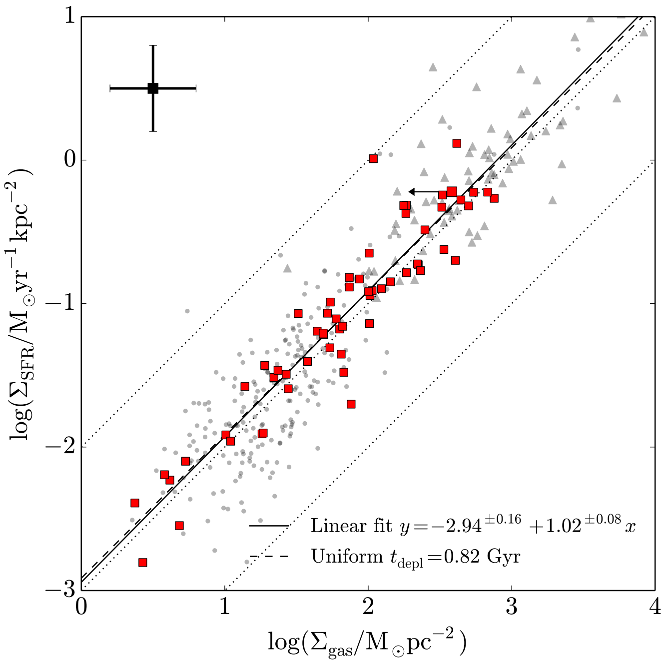

Fig. 6: Kennicutt-Schmidt relation for the galaxies of the PHIBSS2 sample at $z = 0.5 - 0.8$. The dotted diagonal lines correspond to constant depletion times of 0.1, 1 and 10 Gyr from top to bottom and the 0.3 dex errors assumed to assess the uncertainties are displayed at the upper left. The observed PHIBSS2 $z = 0.4 - 0.8$ data points are indicated by squares and the upper limit by an arrow. The underlying gray points correspond to COLDGASS data (Saintonge et al. 2011a, 2012) and the gray triangles to PHIBSS (Tacconi et al. 2013). The black solid line corresponds to a linear least square fits to the data points; the dashed lines to a uniform depletion time corresponding to the best-fitting value on the KS diagram. The Pearson correlation coefficient is 0.94 while the standard deviation from the linear fit is 0.24 dex.

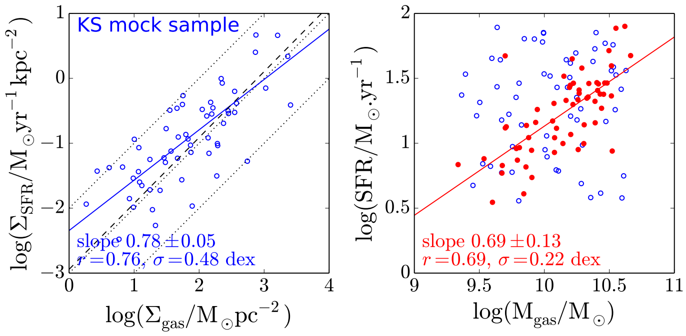

Fig. 7: *Left:* Kennicutt-Schmidt relation for a mock sample where the molecular gas mass and the SFR are not correlated and their logarithms uniformly distributed between the extrema of the PHIBSS2 $z = 0.5 - 0.8$ sample, assuming a Gaussian distribution for $\log(R_{\rm Sersic}/{\rm kpc})$ with mean and standard deviation corresponding to those of the PHIBSS2 sample. The solid blue line corresponds to a fit to the mock data, the dashed line recalls the best fit from Fig. 6 and the dotted lines indicate uniform depletion times of 0.1, 1 and 10 Gyr from top to bottom. *Right:* Correlation between the SFR and the molecular gas mass of the PHIBSS2 $z = 0.5 - 0.8$ together with the corresponding distribution of the non-correlated mock sample. The PHIBSS2 sample and the resulting fit are indicated in red, while the mock sample is displayed as open blue circles.

2010; Murray 2011; Zamora-Avilés et al. 2012; Zamora-Avilés & Vázquez-Semadeni 2014; Meidt et al. 2013; Davies et al. 2014; Utomo et al. 2015). Alternatively, regions within a single galaxy could have different star formation efficiencies (e.g., Freundlich et al. 2013; Cibinel et al. 2017) and the conversion factors used to determine the molecular gas mass and the SFR may also vary from region to region or between galaxies (e.g., Israel 1997; Bolatto et al. 2013). Furthermore, observations in the Milky Way and nearby galaxies reveal that the properties of the molecular gas in GMCs vary considerably from the disk to the central region of a galaxy, in particular in the presence of strong bars (e.g., Oka et al. 2001; Regan et al. 2001; Jogee et al. 2005; Shetty et al. 2012; Kruijssen & Longmore 2013; Colombo et al. 2014; Leroy et al. 2015; Freeman et al. 2017). This variety, which is also expected for the galaxies of the PHIBSS2 sample, is likely to contribute to the scatter in the KS relation since $\Sigma_{\rm gas}$ and $\Sigma_{\rm SFR}$ do not always probe the same regions within a galaxy.

In the absence of separate size estimates for the SFR and molecular gas distributions, we use the half-light radius obtained from a single Sérsic fit $R_{\rm Sersic}$ to estimate both surface densities, which are consequently not independent from each other. To ensure that the striking correlation between $\Sigma_{\rm SFR}$ and $\Sigma_{\rm gas}$ from Fig. 6 does not stem from the dependence between the two variables, we study the KS relation that would be obtained for non-correlated uniform distributions of $\log({\rm M_{gas}/M_\odot})$ and $\log({\rm SFR/M_\odot.yr^{-1}})$ between the extrema of the PHIBSS2 $z = 0.5 - 0.8$ sample. Fig. 7 shows that such distributions would yield a much bigger scatter of about 0.50 dex and a less linear relation. While the figure shows the result for one such distribution, we confirmed the trend both in slope and scatter by reproducing the experiment 1000 times, obtaining slopes, Pearson correlation coefficients and scatters of 0.6 ± 0.1, 0.62 ± 0.08 and 0.48 ± 0.04 respectively. We also note that sticking to the molecular gas mass and the SFR, which are independent variables unlike their surface densities, yields a clear correlation with slope 0.81 ± 0.14, Pearson coefficient 0.77 and residual standard deviation 0.18 dex: the striking KS relation we obtain in Fig. 6 does not result from an artificial correlation induced by the dependency of both surface densities on galaxy size. We do however notice from Fig. 7 that part of the correlation in the KS diagram is due to our selection of MS galaxies excluding starbursts and quenched galaxies and the fact that both surface densities are not independent variables. These issues are relevant for most KS studies and not specific to that presented here.

4.3. Star formation and morphology

To address how morphology affects star formation within the PHIBSS2 $z = 0.5 - 0.8$ sample, we investigate how global physical parameters such as the stellar mass $M_\star$, the molecular gas mas $M_{\rm gas}$ and the SFR as well as derived quantities like the sSFR, the molecular gas depletion time $t_{\rm depl}$ and gas-to-stellar mass ratio $\mu_{\rm gas}$ depend on the bulge-to-total ratio B/T and the total stellar surface density $\Sigma_\star = 0.5 M_\star/\pi R_{\rm Sersic}^2$. Shi et al. (2011) notably show from a large sample of galaxies at different redshifts that the depletion time is a decreasing function of $\Sigma_\star$, which can be understood both in terms of the stellar contribution to the gravitational potential in which stars form and in terms of disk hydrostatic pressure acting on star-forming regions. A high disk pres-

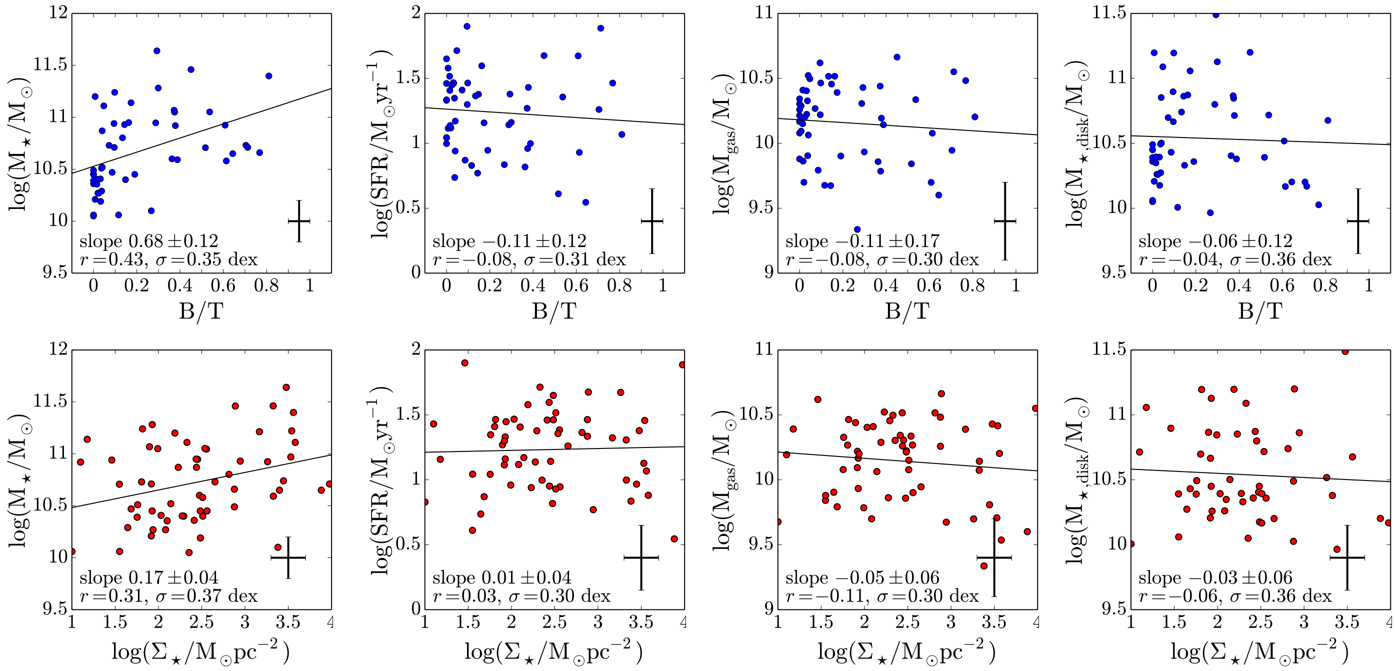

Fig. 8: Dependence of different galaxy parameters on the bulge-to-total ratio B/T within the PHIBSS2 sample at $z = 0.5 - 0.8$. In each panel, we carry out a linear least square fit shown as a black solid line and indicate its slope, assuming 0.3dex errors on the different quantities, as well as the Pearson correlation coefficient (r) and the scatter of the residuals of the best-fitting linear relation (σ). Assumed errors are indicated in the lower right corners.

sure indeed enhances the production of H_2 molecular gas from HI atomic gas and hence contribute to balance stellar feedback (Blitz & Rosolowsky 2004; Schaye & Dalla Vecchia 2008; Shi et al. 2011). To quantify the correlations between the different parameters with B/T and $\Sigma_\star$, we carry out linear least square fits with errors on both axes, determine the Pearson correlation coefficient r between them and indicate the scatter σ of the residuals. B/T and $\Sigma_\star$ are themselves correlated, with a Pearson correlation coefficient $r = 0.67$. As mentioned in section 3.4, most fits with B/T = 1 correspond to cases where the inner structure of the galaxies include spiral arms not well accounted for so we exclude these points from the correlations. As shown in Fig. 8, we find that while the stellar mass increases with B/T and $\Sigma_\star$ (respectively with $r = 0.43$ and 0.31), the SFR and the molecular gas mass do not seem to depend on these parameters (with $|r| \lesssim 0.10$). Derived quantities are consistent with these trends: the sSFR and $\mu_{\rm gas}$ decrease both with B/T and $\Sigma_\star$ (respectively with $r = -0.45$ and -0.49 with B/T, -0.26 and -0.38 with $\Sigma_\star$) while $t_{\rm depl}$ displays no correlation with B/T ($|r| < 0.05$) and a very weak negative correlation of slope -0.06 with $\Sigma_\star$ ($r = -0.17$). We also introduce

$$M_{\star,\rm disk} = (1 - B/T) \times M_\star \tag{12}$$

the stellar mass within the disk, which does not correlate with B/T and $\Sigma_\star$ ($|r| < 0.10$). As can be seen in Fig. A.1, the goodness of the best-fit `galfit` model varies from one galaxy to another, which could affect the correlations with B/T and $\Sigma_\star$. To test how the goodness-of-fit affects these correlations, we also determine Pearson correlation coefficients weighted by the reduced χ^2 of the best-fit models. We find no significant deviation from the trends indicated above (namely, the weighted correlation coefficients with B/T and $\Sigma_\star$ are respectively 0.37 and 0.29 for $\log(M_\star/M_\odot)$, -0.11 and 0.11 for $\log(\mathrm{SFR}/M_\odot\mathrm{yr}^{-1})$, -0.15 and -0.04 for $\log(M_{\rm gas}/M_\odot)$, -0.08 and -0.12 for $\log(M_{\star,\rm disk}/M_\odot)$), advocating relatively robust correlations. The decrease of the sSFR with B/T, which was also observed at low-redshift by Saintonge et al. (2012), can be either interpreted as a decreasing sSFR with bulge growth or as a consequence of the fact that B/T traces the fraction of stars that formed early and are now part of the bulge while the sSFR traces on the contrary the fraction of stars that formed recently. Similarly, the total molecular gas-to-stellar mass ratio and the corresponding gas fraction decrease with B/T and $\Sigma_\star$ in accordance to low and high redshift measurements where morphology is probed by the concentration parameter and the Sérsic index (Saintonge et al. 2011a; Papovich et al. 2015). Assuming an evolutionary sequence from small to high B/T for the same objects, the fact that the molecular gas mass does not vary with B/T and $\Sigma_\star$ suggests an ongoing supply of fresh molecular gas while the stellar bulge assembles, which could stem from mergers, infall from the cosmic web through streams of cold gas penetrating inside the hot circumgalactic medium (Dekel et al. 2009a) or from efficient transformation from atomic to molecular gas owing to the pressure increase (Blitz & Rosolowsky 2004). This continuing supply of gas would be reflected on the disk gas-to-stellar mass ratio $\mu_{\rm gas,disk} = M_{\rm gas}/M_{\star,\rm disk}$, which does neither correlate with B/T nor $\Sigma_\star$ ($|r| < 0.05$). Without invoking an evolutionary sequence, the absence of correlation for the molecular gas mass, the SFR and hence the depletion time with B/T might indicate relatively uniform star formation processes in a given redshift bin, irrespective of the past star formation history traced by B/T.

Contrarily to morphological quenching scenarios (Martig et al. 2009) and observations in the nearby Universe (Saintonge et al. 2011b), we do not observe any variation of the depletion time with B/T and $\Sigma_\star$ ($|r| < 0.05$). This variation is expected to be more pronounced when the gas fraction drops below 20% (Martig et al. 2009; Gobat et al. 2018), so we separately searched for it in galaxies with $f_{\rm gas} < 20\%$ but did not observe any significant variation of the depletion time with B/T and $\Sigma_\star$. Part of this negative result can come from the fact that Gobat et al. (2018) rely on dust observations encompassing both molecular and atomic gas, while we only have access to the molecular gas. When B/T increases, more gas may remain atomic instead of molecular as the bulge stabilizes the disk against gravitational collapse and fragmentation, so the total depletion time including both molecular and atomic components may increase without any increase of the molecular gas depletion time. More importantly, Gobat et al. (2018) focus on quenched red and dead galaxies well below the MS while PHIBSS2 galaxies are precisely on and around the MS. By selecting star-forming galaxies, we may exclude those with high depletion times. And although our sample does include bulge-dominated galaxies, those are still on the MS and thus potentially atypical with relatively high values of their SFR. For example, they could have become bulge-dominated from mergers or violent disk instabilities recently, both processes being also able to trigger star formation. Morphological quenching and compaction events take time to settle down (Gobat et al. 2018; Dekel et al. 2017, in prep.) and may thus not be observed in the recent bulge-dominated galaxies of our sample.

5. Conclusion

This paper presents the strategy and the $z = 0.5 - 0.8$ results of the PHIBSS2 survey, a four-year legacy program with the IRAM NOEMA interferometer designed to investigate early galaxy evolution from the perspective of the galaxies' molecular gas reservoirs. This survey builds upon the successful PHIBSS program (Tacconi et al. 2010, 2013), which uncovered high gas fractions near the peak epoch of star formation and showed that the cosmic evolution of the star formation rate was mainly driven by the molecular gas reservoirs. The PHIBSS and PHIBSS2 surveys probe a representative sample of star-forming main sequence galaxies drawn from well-studied parent catalogs in the COSMOS, AEGIS and GOODS-North cosmological deep fields. While PHIBSS focused on galaxies at $z = 1.2$ and 2.2 on and above the MS, PHIBSS2 significantly enlarges the sample by probing the build-up epoch at $z > 2$, the winding-down of star formation at $z < 0.8$ and galaxies below the MS at $z = 1 - 1.6$. It aims at homogeneous coverage of the MS in the $M_\star$-SFR plane (Fig. 1), without morphological selection. With a total of more than 120 sources, PHIBSS2 significantly adds to the number of molecular gas observations above $z = 0.5$. Together with PHIBSS, it thus provides a benchmark sample of near MS galaxies at different redshifts with molecular gas measurements, which can be used for further CO and dust continuum follow-ups at high resolution with ALMA and NOEMA as well as for other complementary observations.

In this paper we present the CO(2-1) molecular gas observations obtained at $z = 0.5 - 0.8$ as part of the PHIBSS2 survey, reporting 60 detections from a sample of 61 galaxies (Tables 2 and 3). We determine the molecular gas masses, gas fractions, gas-to-stellar mass ratios and depletion times of these galaxies and carry out single Sérsic and two-component bulge disk fits with the 2D morphology fitting code `galfit` to obtain the half-light radii of the galaxies and their components as well as their bulge-to-total luminosity ratios, molecular gas mass and SFR surface densities. The molecular gas-to-stellar mass ratio, gas fraction and depletion time respectively yield values between $0.03 - 1.79$, $0.03 - 0.64$ and $0.11 - 3.82$ Gyr with medians $\widetilde{\mu_{\rm gas}} = 0.28 \pm 0.04$, $\widetilde{f_{\rm gas}} = 0.22 \pm 0.02$ and $\widetilde{t_{\rm depl}} = 0.84 \pm 0.07$ Gyr (Table 3 and Fig. 3). These values are consistent with the observed increase of the gas fraction and slight decrease of the depletion time with redshift (Tacconi et al. 2013, 2018; Genzel et al. 2015). They are indeed in excellent agreement with the scaling relations of the depletion time and the gas fraction as a function of stellar mass, offset from the MS and galaxy size established by Tacconi et al. (2018) within a much more comprehensive sample of about 1400 galaxies between $z = 0$ and $z = 4.6$ (Fig. 5). We show that the Kennicutt-Schmidt relation between molecular gas and SFR surface densities within our sample is strikingly linear (Fig. 6), which argues in favor of uniform star formation timescales within galaxies at any given epoch. In terms of morphology, we study the dependence of different global parameters including the depletion time and the molecular gas fraction on the bulge-to-total ratio B/T and the stellar surface density $\Sigma_\star$ (Fig. 8). In particular, the total molecular gas mass, the SFR as well as the disk stellar mass and molecular gas fraction do not seem to depend on these two quantities. This either suggests an ongoing supply of fresh gas to the disk while the stellar bulge assembles or that star formation proceeds irrespectively of the past star formation history traced by B/T. We find no strong evidence for morphological quenching, which we would expect to manifest as a dependence of the molecular gas depletion time on B/T and $\Sigma_\star$. Our sample however only focuses on star-forming galaxies within the scatter of the MS while probing morphological quenching might request including galaxies well below it. Hence, this should not be interpreted as evidence against morphological quenching in general.

Acknowledgements. The authors acknowledge the particularly careful reading of the anonymous referee, which greatly contributed to improve this article. J. F. would like to thank Benoît Epinat and Marc Huertas Company for their advice using Galfit, Avishai Dekel, Sandy Faber, Joel Primack, Sandro Tacchella and Sharon Lapiner for interesting discussions and insights. The observations presented here were carried out at the IRAM Plateau de Bure/NOEMA interferometer and we are grateful to the astronomers on duty and telescope operators for the quality of the data. This study makes use of data from AEGIS, a multiwavelength sky survey conducted with the Chandra, GALEX, Hubble, Keck, CFHT, MMT, Subaru, Palomar, Spitzer, VLA, and other telescopes and supported in part by the NSF, NASA, and the STFC. It is also based on data products from observations made with ESO Telescopes at the La Silla Paranal Observatory under ESO programme ID 179.A-2005 and on data products produced by TERAPIX and the Cambridge Astronomy Survey Unit on behalf of the UltraVISTA consortium. It further uses observations made with the Spitzer Space Telescope, which is operated by the Jet Propulsion Laboratory, California Institute of Technology under a contract with NASA. Finally, this work was based in part on observations made with the NASA/ESA Hubble Space Telescope, and obtained from the Hubble Legacy Archive, which is a collaboration between the Space Telescope Science Institute (STScI/NASA), the Space Telescope European Coordinating Facility (ST-ECF/ESA) and the Canadian Astronomy Data Centre (CADC/NRC/CSA).

References

Abdo, A. A., Ackermann, M., Ajello, M., et al. 2010, ApJ, 710, 133
Aravena, M., Carilli, C., Daddi, E., et al. 2010, ApJ, 718, 177
Baldry, I. K., Glazebrook, K., Brinkmann, J., et al. 2004, ApJ, 600, 681
Bauermeister, A., Blitz, L., Bolatto, A., et al. 2013, ApJ, 768, 132
Bauermeister, A., Blitz, L., & Ma, C.-P. 2010, ApJ, 717, 323
Bigiel, F., Leroy, A., Walter, F., et al. 2008, AJ, 136, 2846
Bigiel, F., Leroy, A. K., Walter, F., et al. 2011, ApJ, 730, L13
Birnboim, Y. & Dekel, A. 2003, MNRAS, 345, 349
Blitz, L. & Rosolowsky, E. 2004, ApJ, 612, L29
Bolatto, A. D., Leroy, A. K., Rosolowsky, E., Walter, F., & Blitz, L. 2008, ApJ, 686, 948
Bolatto, A. D., Wolfire, M., & Leroy, A. K. 2013, ARA&A, 51, 207
Bothwell, M. S., Smail, I., Chapman, S. C., et al. 2013, MNRAS, 429, 3047
Bouché, N., Dekel, A., Genzel, R., et al. 2010, ApJ, 718, 1001
Bouwens, R. J., Illingworth, G. D., Oesch, P. A., et al. 2010, ApJ, 709, L133
Brammer, G. B., van Dokkum, P. G., Franx, M., et al. 2012, ApJS, 200, 13
Brinchmann, J., Charlot, S., White, S. D. M., et al. 2004, MNRAS, 351, 1151
Bruce, V. A., Dunlop, J. S., Cirasuolo, M., et al. 2012, MNRAS, 427, 1666
Caputi, K. I., Dole, H., Lagache, G., et al. 2006, ApJ, 637, 727

Catinella, B., Schiminovich, D., Kauffmann, G., et al. 2010, MNRAS, 403, 683
Cattaneo, A., Dekel, A., Devriendt, J., Guiderdoni, B., & Blaizot, J. 2006, MNRAS, 370, 1651
Cibinel, A., Daddi, E., Bournaud, F., et al. 2017, MNRAS, 469, 4683
Cicone, C., Maiolino, R., Sturm, E., et al. 2014, A&A, 562, A21
Colombo, D., Hughes, A., Schinnerer, E., et al. 2014, ApJ, 784, 3
Combes, F. 1991, ARA&A, 29, 195
Combes, F., García-Burillo, S., Braine, J., et al. 2011, A&A, 528, A124
Combes, F., García-Burillo, S., Braine, J., et al. 2013, A&A, 550, A41
Combes, F., Maoli, R., & Omont, A. 1999, A&A, 345, 369
Conroy, C. & Wechsler, R. H. 2009, ApJ, 696, 620
Contini, T., Epinat, B., Bouché, N., et al. 2016, A&A, 591, A49
Cox, P. 2011, IRAM Annual Reports, http://www.iram-institute.org/medias/uploads/file/PDFs/IRAM_2011.pdf
Cucciati, O., Tresse, L., Ilbert, O., et al. 2012, A&A, 539, A31
Daddi, E., Bournaud, F., Walter, F., et al. 2010a, ApJ, 713, 686
Daddi, E., Dannerbauer, H., Elbaz, D., et al. 2008, ApJ, 673, L21
Daddi, E., Dannerbauer, H., Liu, D., et al. 2015, A&A, 577, A46
Daddi, E., Dickinson, M., Morrison, G., et al. 2007, ApJ, 670, 156
Daddi, E., Elbaz, D., Walter, F., et al. 2010b, ApJ, 714, L118
Daddi, E., Renzini, A., Pirzkal, N., et al. 2005, ApJ, 626, 680
Dame, T. M., Hartmann, D., & Thaddeus, P. 2001, ApJ, 547, 792
Damen, M., Labbé, I., Franx, M., et al. 2009, ApJ, 690, 937
Dannerbauer, H., Daddi, E., Riechers, D. A., et al. 2009, ApJ, 698, L178
Davé, R., Finlator, K., & Oppenheimer, B. D. 2011a, MNRAS, 416, 1354
Davé, R., Finlator, K., & Oppenheimer, B. D. 2012, MNRAS, 421, 98
Davé, R., Oppenheimer, B. D., & Finlator, K. 2011b, MNRAS, 415, 11
Davies, R. I., Maciejewski, W., Hicks, E. K. S., et al. 2014, ApJ, 792, 101
Davis, M., Guhathakurta, P., Konidaris, N. P., et al. 2007, ApJ, 660, L1
Decarli, R., Walter, F., Aravena, M., et al. 2016, ApJ, 833, 70
Dekel, A. & Birnboim, Y. 2006, MNRAS, 368, 2
Dekel, A., Birnboim, Y., Engel, G., et al. 2009a, Nature, 457, 451
Dekel, A. & Burkert, A. 2014, MNRAS, 438, 1870
Dekel, A., Lapiner, S., Kretschmer, M., et al. 2017, in prep.
Dekel, A. & Mandelker, N. 2014, MNRAS, 444, 2071
Dekel, A., Sari, R., & Ceverino, D. 2009b, ApJ, 703, 785
Dekel, A., Zolotov, A., Tweed, D., et al. 2013, MNRAS, 435, 999
Dessauges-Zavadsky, M., Zamojski, M., Rujopakarn, W., et al. 2017, A&A, 605, A81
Dickman, R. L., Snell, R. L., & Schloerb, F. P. 1986, ApJ, 309, 326
Elbaz, D., Daddi, E., Le Borgne, D., et al. 2007, A&A, 468, 33
Elbaz, D., Dickinson, M., Hwang, H. S., et al. 2011, A&A, 533, A119
Erb, D. K., Steidel, C. C., Shapley, A. E., et al. 2006, ApJ, 646, 107
Feldmann, R. 2013, MNRAS, 433, 1910
Feruglio, C., Maiolino, R., Piconcelli, E., et al. 2010, A&A, 518, L155
Förster Schreiber, N. M., Genzel, R., Bouché, N., et al. 2009, ApJ, 706, 1364
Förster Schreiber, N. M., Genzel, R., Lehnert, M. D., et al. 2006, ApJ, 645, 1062
Förster Schreiber, N. M., Genzel, R., Newman, S. F., et al. 2014, ApJ, 787, 38
Freeman, K. C. 1970, ApJ, 160, 811
Freeman, K. C. 2008, in IAU Symposium, Vol. 245, Formation and Evolution of Galaxy Bulges, ed. M. Bureau, E. Athanassoula, & B. Barbuy, 3–10
Freeman, P., Rosolowsky, E., Kruijssen, J. M. D., Bastian, N., & Adamo, A. 2017, MNRAS, 468, 1769
Freundlich, J., Combes, F., Tacconi, L. J., et al. 2013, A&A, 553, A130
Geach, J. E., Hickox, R. C., Diamond-Stanic, A. M., et al. 2014, Nature, 516, 68
Geach, J. E., Smail, I., Moran, S. M., et al. 2011, ApJ, 730, L19
Genel, S., Bouché, N., Naab, T., Sternberg, A., & Genzel, R. 2010, ApJ, 719, 229
Genzel, R., Burkert, A., Bouché, N., et al. 2008, ApJ, 687, 59
Genzel, R., Newman, S., Jones, T., et al. 2011, ApJ, 733, 101
Genzel, R., Tacconi, L. J., Combes, F., et al. 2012, ApJ, 746, 69
Genzel, R., Tacconi, L. J., Eisenhauer, F., et al. 2006, Nature, 442, 786
Genzel, R., Tacconi, L. J., Gracia-Carpio, J., et al. 2010, MNRAS, 407, 2091
Genzel, R., Tacconi, L. J., Kurk, J., et al. 2013, ApJ, 773, 68
Genzel, R., Tacconi, L. J., Lutz, D., et al. 2015, ApJ, 800, 20
Giavalisco, M., Ferguson, H. C., Koekemoer, A. M., et al. 2004, ApJ, 600, L93
Gobat, R., Daddi, E., Magdis, G., et al. 2018, Nature Astronomy, 2, 239
Grenier, I. A., Casandjian, J.-M., & Terrier, R. 2005, Science, 307, 1292
Greve, T. R., Bertoldi, F., Smail, I., et al. 2005, MNRAS, 359, 1165
Grogin, N. A., Kocevski, D. D., Faber, S. M., et al. 2011, ApJS, 197, 35
Guilloteau, S., Delannoy, J., Downes, D., et al. 1992, A&A, 262, 624
Häussler, B., McIntosh, D. H., Barden, M., et al. 2007, ApJS, 172, 615
Huang, M.-L. & Kauffmann, G. 2014, MNRAS, 443, 1329
Hwang, H. S., Elbaz, D., Magdis, G., et al. 2010, MNRAS, 409, 75
Israel, F. P. 1997, A&A, 328, 471
Ivison, R. J., Papadopoulos, P. P., Smail, I., et al. 2011, MNRAS, 412, 1913
Jogee, S., Scoville, N., & Kenney, J. D. P. 2005, ApJ, 630, 837
Juneau, S., Dickinson, M., Bournaud, F., et al. 2013, ApJ, 764, 176
Kennicutt, R. C. & Evans, N. J. 2012, ARA&A, 50, 531
Kennicutt, Jr., R. C. 1998a, ARA&A, 36, 189
Kennicutt, Jr., R. C. 1998b, ApJ, 498, 541
Kereš, D., Katz, N., Fardal, M., Davé, R., & Weinberg, D. H. 2009, MNRAS, 395, 160
Kereš, D., Katz, N., Weinberg, D. H., & Davé, R. 2005, MNRAS, 363, 2
Koekemoer, A. M., Faber, S. M., Ferguson, H. C., et al. 2011, ApJS, 197, 36
Kruijssen, J. M. D. & Longmore, S. N. 2013, MNRAS, 435, 2598
Lada, C. J., Lombardi, M., & Alves, J. F. 2010, ApJ, 724, 687
Lagos, C. d. P., Crain, R. A., Schaye, J., et al. 2015, MNRAS, 452, 3815
Laigle, C., McCracken, H. J., Ilbert, O., et al. 2016, ApJS, 224, 24
Lang, P., Wuyts, S., Somerville, R. S., et al. 2014, ApJ, 788, 11
Leroy, A. K., Bolatto, A., Gordon, K., et al. 2011, ApJ, 737, 12
Leroy, A. K., Bolatto, A. D., Ostriker, E. C., et al. 2015, ApJ, 801, 25
Leroy, A. K., Walter, F., Bigiel, F., et al. 2009, AJ, 137, 4670
Leroy, A. K., Walter, F., Brinks, E., et al. 2008, AJ, 136, 2782
Leroy, A. K., Walter, F., Sandstrom, K., et al. 2013, AJ, 146, 19
Lilly, S. J., Carollo, C. M., Pipino, A., Renzini, A., & Peng, Y. 2013, ApJ, 772, 119
Lilly, S. J., Le Brun, V., Maier, C., et al. 2009, ApJS, 184, 218
Lilly, S. J., Le Fèvre, O., Renzini, A., et al. 2007, ApJS, 172, 70
Lombardi, M., Alves, J., & Lada, C. J. 2010, A&A, 519, L7
Madau, P. & Dickinson, M. 2014, ARA&A, 52, 415
Magdis, G. E., Daddi, E., Béthermin, M., et al. 2012a, ApJ, 760, 6
Magdis, G. E., Daddi, E., Sargent, M., et al. 2012b, ApJ, 758, L9
Magnelli, B., Elbaz, D., Chary, R. R., et al. 2009, A&A, 496, 57
Magnelli, B., Saintonge, A., Lutz, D., et al. 2012, A&A, 548, A22
Martig, M., Bournaud, F., Teyssier, R., & Dekel, A. 2009, ApJ, 707, 250
Masci, F. 2011, http://wise2.ipac.caltech.edu/staff/fmasci/UpperLimits_FM2011.pdf
Meidt, S. E., Schinnerer, E., García-Burillo, S., et al. 2013, ApJ, 779, 45
Momcheva, I. G., Brammer, G. B., van Dokkum, P. G., et al. 2016, ApJS, 225, 27
Mullaney, J. R., Pannella, M., Daddi, E., et al. 2012, MNRAS, 419, 95
Murray, N. 2011, ApJ, 729, 133
Murray, N., Quataert, E., & Thompson, T. A. 2010, ApJ, 709, 191
Newman, S. F., Shapiro Griffin, K., Genzel, R., et al. 2012, ApJ, 752, 111
Noeske, K. G., Weiner, B. J., Faber, S. M., et al. 2007, ApJ, 660, L43
Ocvirk, P., Pichon, C., & Teyssier, R. 2008, MNRAS, 390, 1326
Oka, T., Hasegawa, T., Sato, F., et al. 2001, ApJ, 562, 348
Onodera, S., Kuno, N., Tosaki, T., et al. 2010, ApJ, 722, L127
Papadopoulos, P. P., van der Werf, P., Xilouris, E., Isaak, K. G., & Gao, Y. 2012a, ApJ, 751, 10
Papadopoulos, P. P., van der Werf, P. P., Xilouris, E. M., et al. 2012b, MNRAS, 426, 2601
Papovich, C., Labbé, I., Quadri, R., et al. 2015, ApJ, 803, 26
Peng, C. Y., Ho, L. C., Impey, C. D., & Rix, H.-W. 2002, AJ, 124, 266
Peng, C. Y., Ho, L. C., Impey, C. D., & Rix, H.-W. 2010a, AJ, 139, 2097
Peng, Y.-j., Lilly, S. J., Kovač, K., et al. 2010b, ApJ, 721, 193
Peng, Y.-j. & Maiolino, R. 2014, MNRAS, 443, 3643
Pettini, M. & Pagel, B. E. J. 2004, MNRAS, 348, L59
Pettini, M., Steidel, C. C., Adelberger, K. L., Dickinson, M., & Giavalisco, M. 2000, ApJ, 528, 96
Reddy, N. A. & Steidel, C. C. 2009, ApJ, 692, 778
Regan, M. W., Thornley, M. D., Helfer, T. T., et al. 2001, ApJ, 561, 218
Renzini, A. & Peng, Y.-j. 2015, ApJ, 801, L29
Rodighiero, G., Cimatti, A., Gruppioni, C., et al. 2010, A&A, 518, L25
Rodighiero, G., Daddi, E., Baronchelli, I., et al. 2011, ApJ, 739, L40
Roediger, J. C. & Courteau, S. 2015, MNRAS, 452, 3209
Saintonge, A., Kauffmann, G., Kramer, C., et al. 2011a, MNRAS, 415, 32
Saintonge, A., Kauffmann, G., Wang, J., et al. 2011b, MNRAS, 415, 61
Saintonge, A., Lutz, D., Genzel, R., et al. 2013, ApJ, 778, 2
Saintonge, A., Tacconi, L. J., Fabello, S., et al. 2012, ApJ, 758, 73
Sandstrom, K. M., Leroy, A. K., Walter, F., et al. 2013, ApJ, 777, 5
Santini, P., Fontana, A., Grazian, A., et al. 2009, A&A, 504, 751
Sargent, M. T., Béthermin, M., Daddi, E., & Elbaz, D. 2012, ApJ, 747, L31
Schaye, J. & Dalla Vecchia, C. 2008, MNRAS, 383, 1210
Schiminovich, D., Wyder, T. K., Martin, D. C., et al. 2007, ApJS, 173, 315
Schinnerer, E., Weiß, A., Aalto, S., & Scoville, N. Z. 2010, ApJ, 719, 1588
Schmidt, M. 1959, ApJ, 129, 243
Schreiber, C., Pannella, M., Elbaz, D., et al. 2015, A&A, 575, A74
Schruba, A., Leroy, A. K., Walter, F., et al. 2011, AJ, 142, 37
Schruba, A., Leroy, A. K., Walter, F., Sandstrom, K., & Rosolowsky, E. 2010, ApJ, 722, 1699
Schuster, K.-F. 2014, IRAM Annual Reports, http://www.iram-institute.org/medias/uploads/IRAM_2014.pdf
Scoville, N., Aussel, H., Brusa, M., et al. 2007, ApJS, 172, 1
Scoville, N. & Young, J. S. 1983, ApJ, 265, 148
Sersic, J. L. 1968, Atlas de galaxias australes
Sharon, C. E., Riechers, D. A., Hodge, J., et al. 2016, ApJ, 827, 18
Shetty, R., Beaumont, C. N., Burton, M. G., Kelly, B. C., & Klessen, R. S. 2012, MNRAS, 425, 720
Shi, Y., Helou, G., Yan, L., et al. 2011, ApJ, 733, 87

Silverman, J. D., Daddi, E., Rodighiero, G., et al. 2015, ApJ, 812, L23

Skelton, R. E., Whitaker, K. E., Momcheva, I. G., et al. 2014, ApJS, 214, 24

Solomon, P. M. & Barrett, J. W. 1991, in IAU Symposium, Vol. 146, Dynamics of Galaxies and Their Molecular Cloud Distributions, ed. F. Combes & F. Casoli, 235

Solomon, P. M., Downes, D., Radford, S. J. E., & Barrett, J. W. 1997, ApJ, 478, 144

Solomon, P. M., Rivolo, A. R., Barrett, J., & Yahil, A. 1987, ApJ, 319, 730

Speagle, J. S., Steinhardt, C. L., Capak, P. L., & Silverman, J. D. 2014, ApJS, 214, 15

Stark, D. P., Swinbank, A. M., Ellis, R. S., et al. 2008, Nature, 455, 775

Strong, A. W. & Mattox, J. R. 1996, A&A, 308, L21

Strong, A. W., Moskalenko, I. V., Reimer, O., Digel, S., & Diehl, R. 2004, A&A, 422, L47

Sturm, E., González-Alfonso, E., Veilleux, S., et al. 2011, ApJ, 733, L16

Tacchella, S., Dekel, A., Carollo, C. M., et al. 2016a, MNRAS, 457, 2790

Tacchella, S., Dekel, A., Carollo, C. M., et al. 2016b, MNRAS, 458, 242

Tacconi, L. J., Genzel, R., Neri, R., et al. 2010, Nature, 463, 781

Tacconi, L. J., Genzel, R., Saintonge, A., et al. 2018, ApJ, 853, 179

Tacconi, L. J., Genzel, R., Smail, I., et al. 2008, ApJ, 680, 246

Tacconi, L. J., Neri, R., Chapman, S. C., et al. 2006, ApJ, 640, 228

Tacconi, L. J., Neri, R., Genzel, R., et al. 2013, ApJ, 768, 74

Utomo, D., Blitz, L., Bolatto, A., Wong, T., & Vogel, S. 2015, IAU General Assembly, 22, 57914

van der Wel, A., Bell, E. F., Häussler, B., et al. 2012, ApJS, 203, 24

van der Wel, A., Franx, M., van Dokkum, P. G., et al. 2014, ApJ, 788, 28

Weiner, B. J., Coil, A. L., Prochaska, J. X., et al. 2009, ApJ, 692, 187

Whitaker, K. E., Franx, M., Leja, J., et al. 2014, ApJ, 795, 104

Whitaker, K. E., van Dokkum, P. G., Brammer, G., & Franx, M. 2012, ApJ, 754, L29

Wisnioski, E., Förster Schreiber, N. M., Wuyts, S., et al. 2015, ApJ, 799, 209

Wolfire, M. G., Hollenbach, D., & McKee, C. F. 2010, ApJ, 716, 1191

Wuyts, E., Kurk, J., Förster Schreiber, N. M., et al. 2014, ApJ, 789, L40

Wuyts, S., Förster Schreiber, N. M., Lutz, D., et al. 2011a, ApJ, 738, 106

Wuyts, S., Förster Schreiber, N. M., van der Wel, A., et al. 2011b, ApJ, 742, 96

Wuyts, S., Labbé, I., Förster Schreiber, N. M., et al. 2008, ApJ, 682, 985

Wyse, R. F. G., Gilmore, G., & Franx, M. 1997, ARA&A, 35, 637

Young, J. S. 2000, in Astronomical Society of the Pacific Conference Series, Vol. 218, Mapping the Hidden Universe: The Universe behind the Mily Way - The Universe in HI, ed. R. C. Kraan-Korteweg, P. A. Henning, & H. Andernach, 321

Young, J. S. & Scoville, N. 1982, ApJ, 258, 467

Young, J. S. & Scoville, N. Z. 1991, ARA&A, 29, 581

Zamora-Avilés, M. & Vázquez-Semadeni, E. 2014, ApJ, 793, 84

Zamora-Avilés, M., Vázquez-Semadeni, E., & Colín, P. 2012, ApJ, 751, 77

Zoccali, M., Renzini, A., Ortolani, S., et al. 2003, A&A, 399, 931

Zolotov, A., Dekel, A., Mandelker, N., et al. 2015, MNRAS, 450, 2327

[1] LERMA, Observatoire de Paris, PSL Research University, CNRS, Sorbonne Universités, UPMC Univ. Paris 06, F-75014, Paris, France
[2] Collège de France, Paris, France
[3] Centre for Astrophysics and Planetary Science, Racah Institute of Physics, The Hebrew University, Jerusalem 91904 Israel
[4] Max-Planck-Institute für extraterrestrische Physik (MPE), Giessenbachstrasse 1, 85748 Garching, Germany
[5] Dept. of Physics, Le Conte Hall, University of California, CA 94720 Berkeley, USA
[6] Dept. of Astronomy, Campbell Hall, University of California, CA 94720 Berkeley, USA
[7] Observatorio Astronómico Nacional - OAN, Apartado 1143, 28800 Alcalá de Henares, Madrid, Spain
[8] IRAM, 300 rue de la Piscine, F-38406 St. Martin d'Heres, Grenoble, France
[9] Institut de Recherche en Astrophysique et Planétologie – IRAP, CNRS, Université de Toulouse, UPS-OMP, 14, avenue E. Belin, 31400 Toulouse, France
[10] Dept. of Astronomy, University of Maryland, College Park, MD 20742-2421, USA
[11] Institute for Astronomy, Department of Physics, ETH Zurich, CH-8093 Zurich, Switzerland
[12] CEA, IRFU, SAp, 91191 Gif-sur-Yvette, France
[13] Universitätsternwarte der Ludwig-Maximiliansuniversität, Scheinerstrasse 1, 81679 München, Germany, MPG-Fellow at MPE
[14] Dept. of Physics & Astronomy, Frederick Reines Hall, University of California, Irvine, CA 92697, USA
[15] Institut d'Astrophysique de Paris, Sorbonne Université, CNRS, UMR 7095, 98 bis bd Arago, 7014 Paris, France
[16] Scuola Normale Superiore, Piazza dei Cavalieri 7, 56126 Pisa, Italy
[17] Max Planck Institut für Astrophysik, Karl Schwarzshildstrasse 1, D-85748 Garching, Germany
[18] INAF-Osservatorio Astronomico di Padova, Vicolo dell'Osservatorio 5, I-35122 Padova, Italy
[19] Department of Physics and Astronomy, University College London, Gower Street, London WC1E 6BT, UK
[20] School of Physics and Astronomy, Tel Aviv University, Tel Aviv 69978, Israel
[21] Max-Planck-Institut für Astronomie, Königstuhl 17, D-69117 Heidelberg, Germany
[22] Steward Observatory, 933 N. Cherry Ave., University of Arizona, Tucson, AZ 85721-0065, USA
[23] Max-Planck-Institut für Radioastronomie, Auf dem Hügel 69, D-53121 Bonn, Germany
[24] Department of Physics, University of Bath, Claverton Down, Bath, BA2 7AY, UK

Appendix A: HST images and NOEMA CO spectra

Fig. A.1 presents the HST/ACS F814W I-band images, the best-fit two-component bulge disk models obtained with the method outlined in section 3.4 and the corresponding residuals, the radial density profiles and the NOEMA CO(2-1) molecular gas spatially-averaged line spectra for the 61 galaxies of the PHIBSS2 $z = 0.5 - 0.8$ sample.

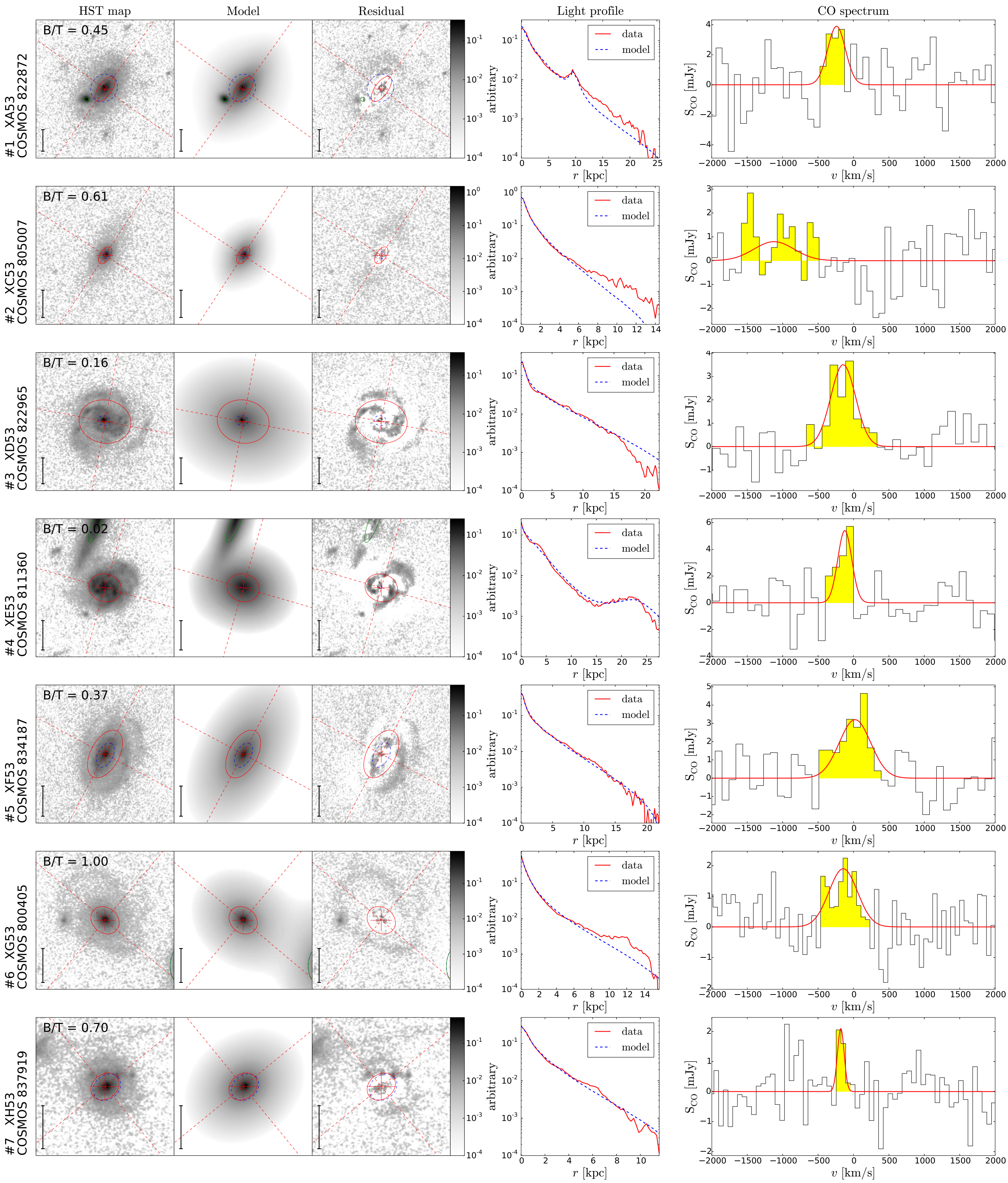

Fig. A.1: HST/ACS F814W I-band image, best-fit two-component bulge disk model, residuals, averaged radial profile and CO spectrum for the different galaxies of the PHIBSS2 $z = 0.5 - 0.8$ sample. For each galaxy, the HST image, the model, the residuals and the radial profile have in the same arbitrary log-scale units. The red and dashed blue ellipses respectively denote the disk and bulge half-light radii, the dashed lines the disk axes and the scale at the bottom left corresponds to 10 kpc. In the light profiles, the solid red line is the averaged profile from the HST image while the dashed blue line that of the model. Green ellipses correspond to neighboring satellites or companions that were simultaneously fitted as single Sérsic light distributions. The CO spectra display a Gaussian fit to the data.

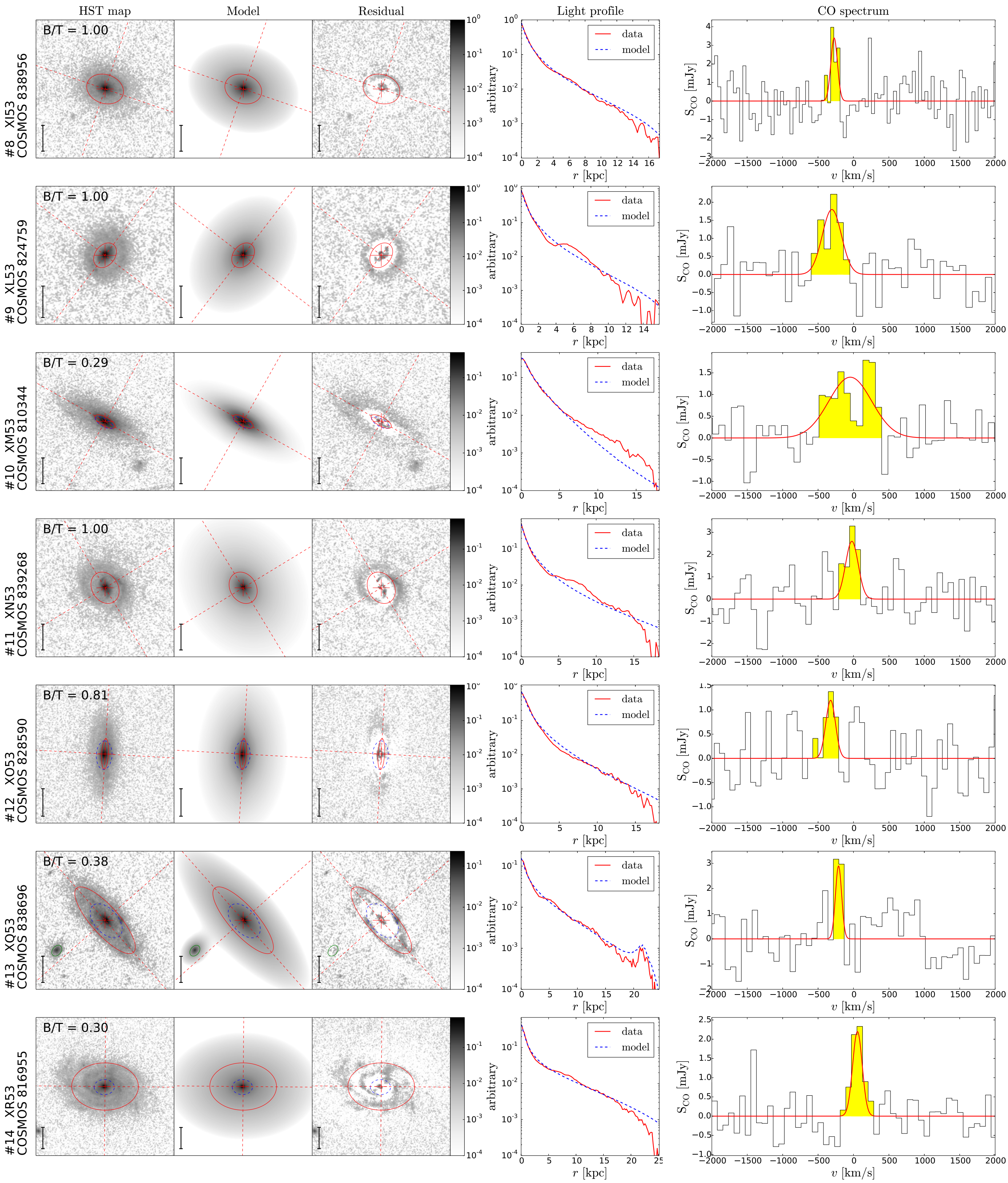
HST map
Model
Residual
Light profile
CO spectrum
#8 XI53
COSMOS 838956
B/T = 1.00
#9 XL53
COSMOS 824759
B/T = 1.00
#10 XM53
COSMOS 810344
B/T = 0.29
#11 XN53
COSMOS 839268
B/T = 1.00
#12 XO53
COSMOS 828590
B/T = 0.81
#13 XQ53
COSMOS 838696
B/T = 0.38
#14 XR53
COSMOS 816955
B/T = 0.30
data
model
arbitrary
r [kpc]
S_CO [mJy]
v [km/s]

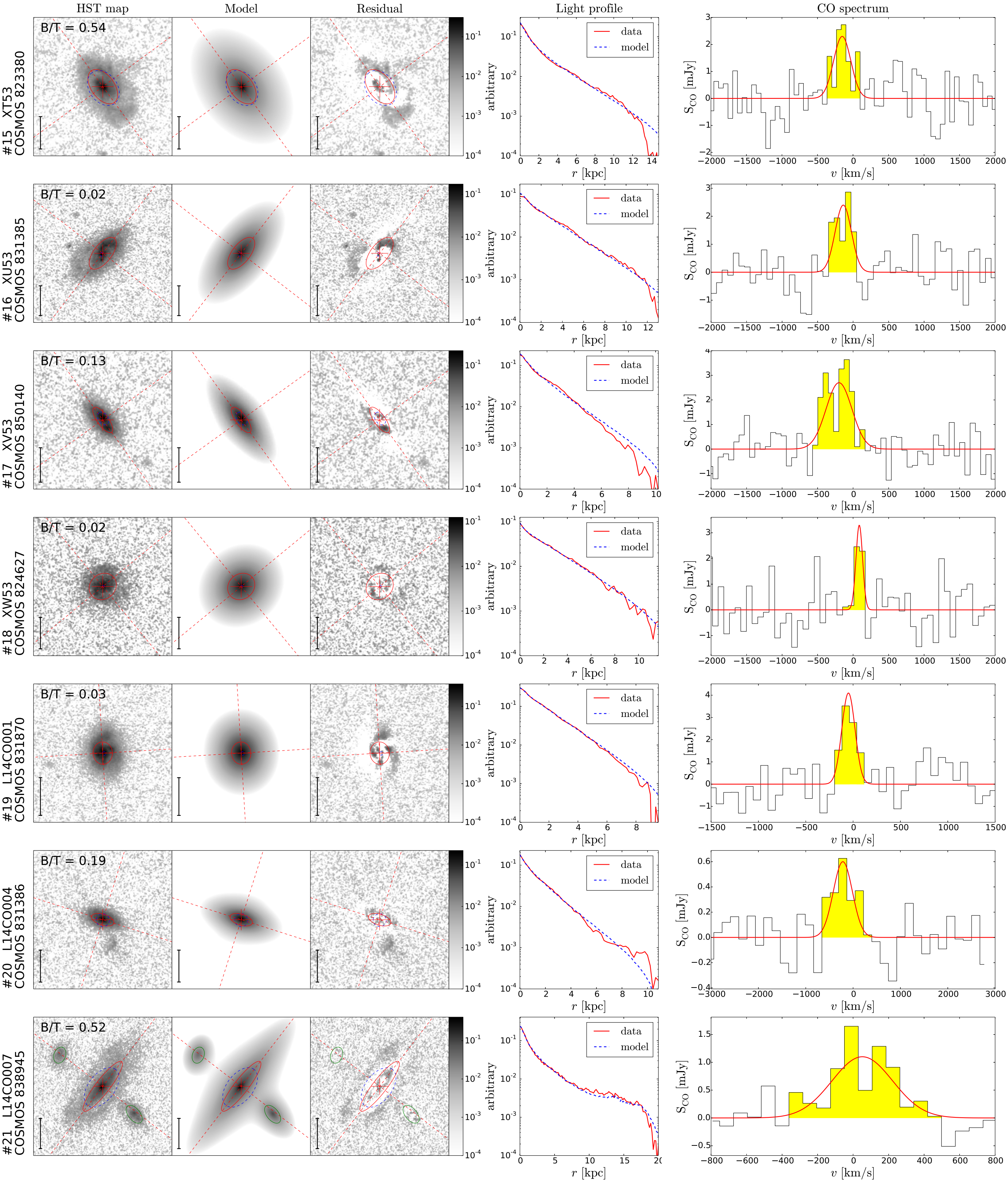
HST map
Model
Residual
Light profile
CO spectrum
#15 XT53 COSMOS 823380
B/T = 0.54
#16 XU53 COSMOS 831385
B/T = 0.02
#17 XV53 COSMOS 850140
B/T = 0.13
#18 XW53 COSMOS 824627
B/T = 0.02
#19 L14CO001 COSMOS 831870
B/T = 0.03
#20 L14CO004 COSMOS 831386
B/T = 0.19
#21 L14CO007 COSMOS 838945
B/T = 0.52
data
model
arbitrary
r [kpc]
S_CO [mJy]
v [km/s]

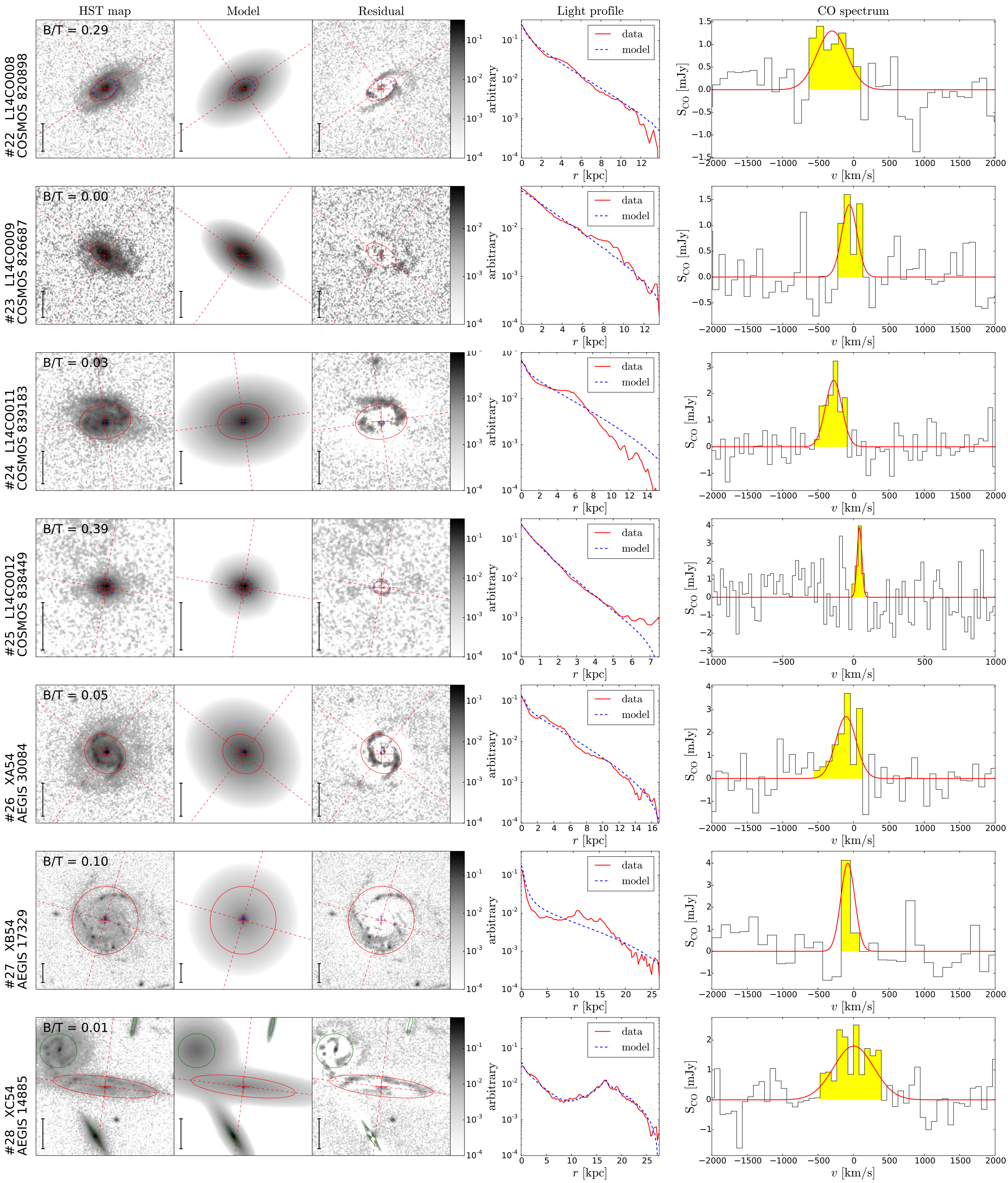
HST map
Model
Residual
Light profile
CO spectrum
#22 L14CO008
COSMOS 820898
B/T = 0.29
#23 L14CO009
COSMOS 826687
B/T = 0.00
#24 L14CO011
COSMOS 839183
B/T = 0.03
#25 L14CO012
COSMOS 838449
B/T = 0.39
#26 XA54
AEGIS 30084
B/T = 0.05
#27 XB54
AEGIS 17329
B/T = 0.10
#28 XC54
AEGIS 14885
B/T = 0.01
data
model
arbitrary
r [kpc]
S_{CO} [mJy]
v [km/s]

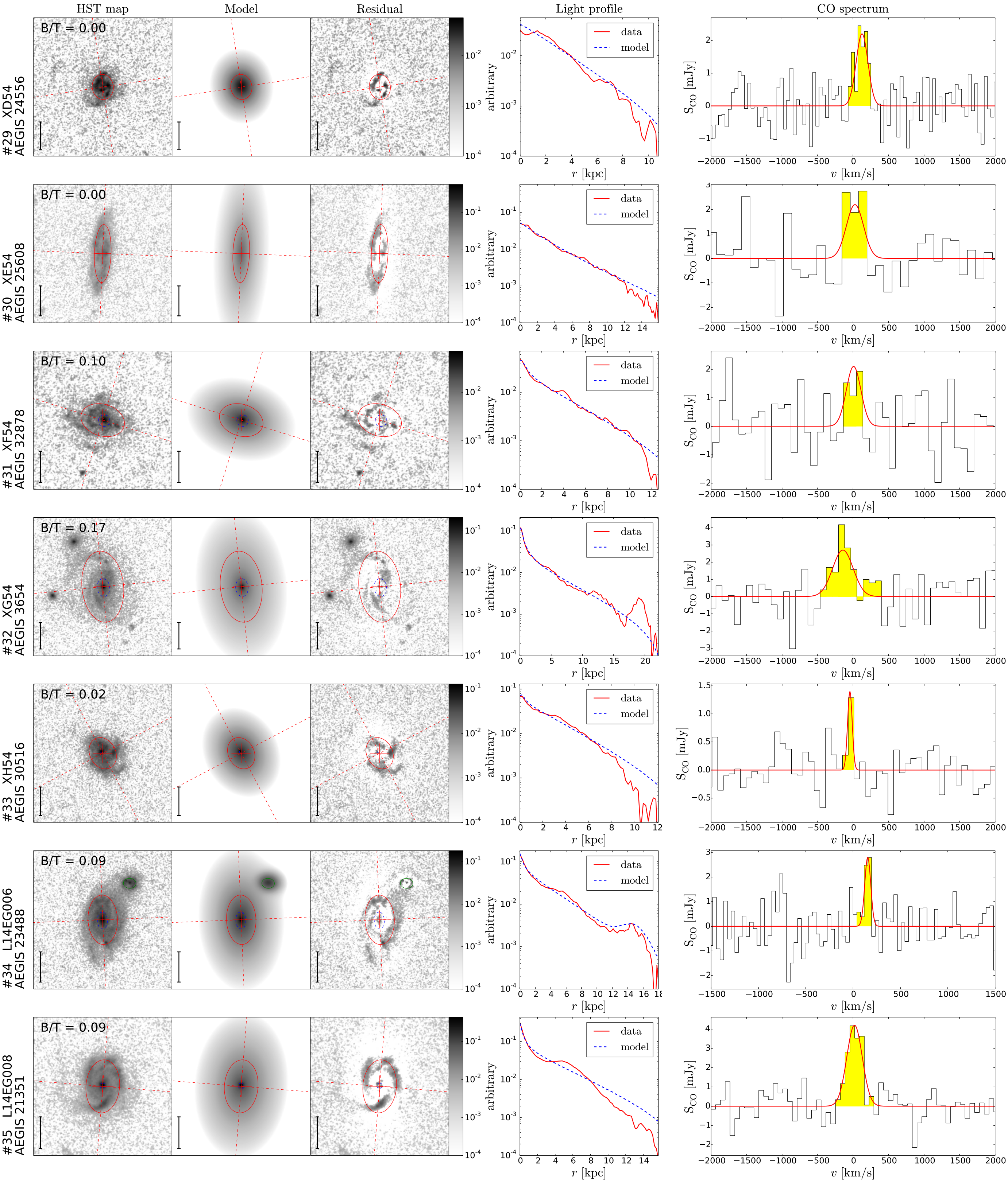
HST map
Model
Residual
Light profile
CO spectrum
#29 XD54 AEGIS 24556
#30 XE54 AEGIS 25608
#31 XF54 AEGIS 32878
#32 XG54 AEGIS 3654
#33 XH54 AEGIS 30516
#34 L14EG006 AEGIS 23488
#35 L14EG008 AEGIS 21351
B/T = 0.00
B/T = 0.00
B/T = 0.10
B/T = 0.17
B/T = 0.02
B/T = 0.09
B/T = 0.09
data
model
arbitrary
r [kpc]
S_CO [mJy]
v [km/s]

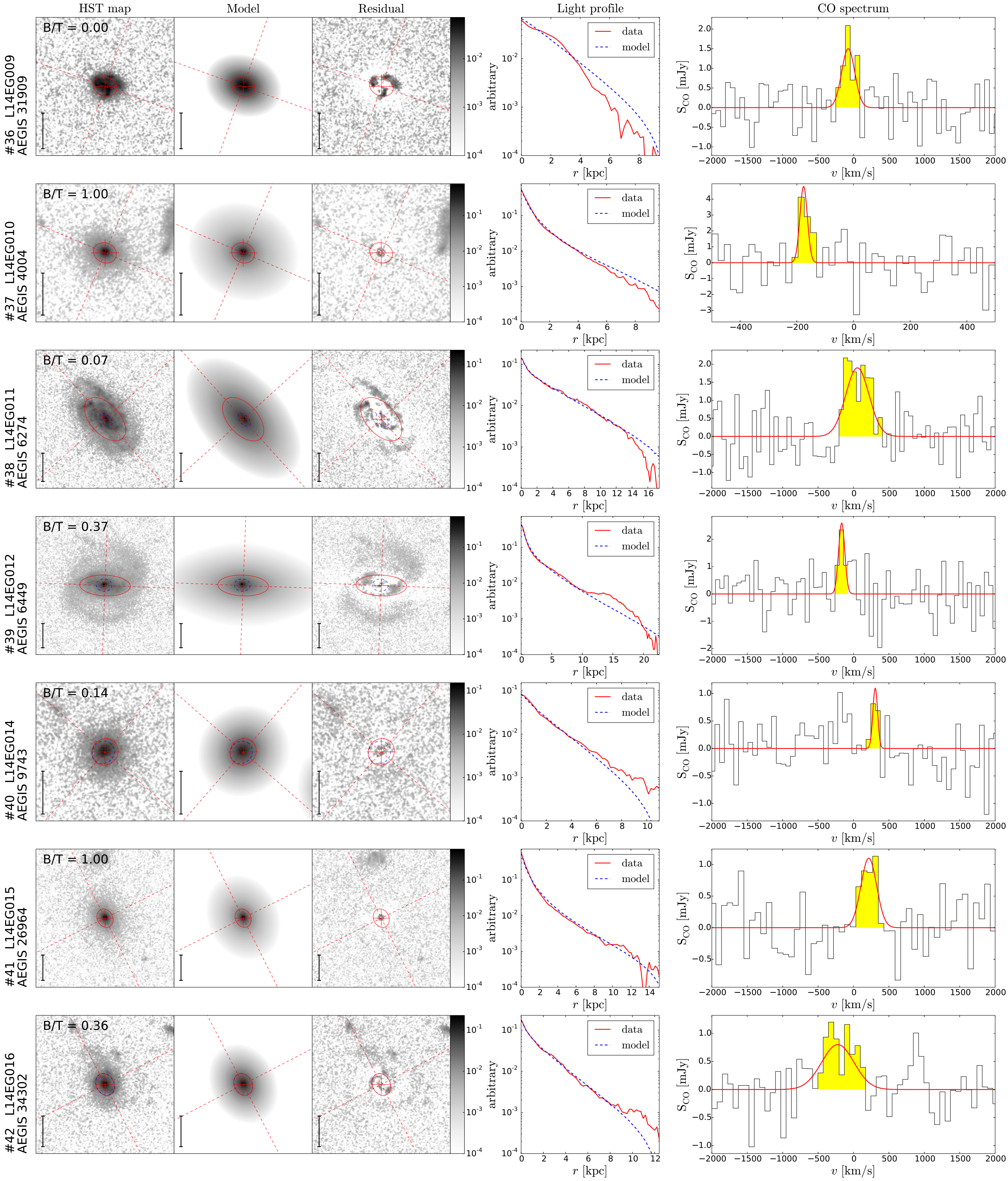
HST map
Model
Residual
Light profile
CO spectrum
#36 L14EG009
AEGIS 31909
B/T = 0.00
#37 L14EG010
AEGIS 4004
B/T = 1.00
#38 L14EG011
AEGIS 6274
B/T = 0.07
#39 L14EG012
AEGIS 6449
B/T = 0.37
#40 L14EG014
AEGIS 9743
B/T = 0.14
#41 L14EG015
AEGIS 26964
B/T = 1.00
#42 L14EG016
AEGIS 34302
B/T = 0.36
data
model
arbitrary
r [kpc]
S_CO [mJy]
v [km/s]

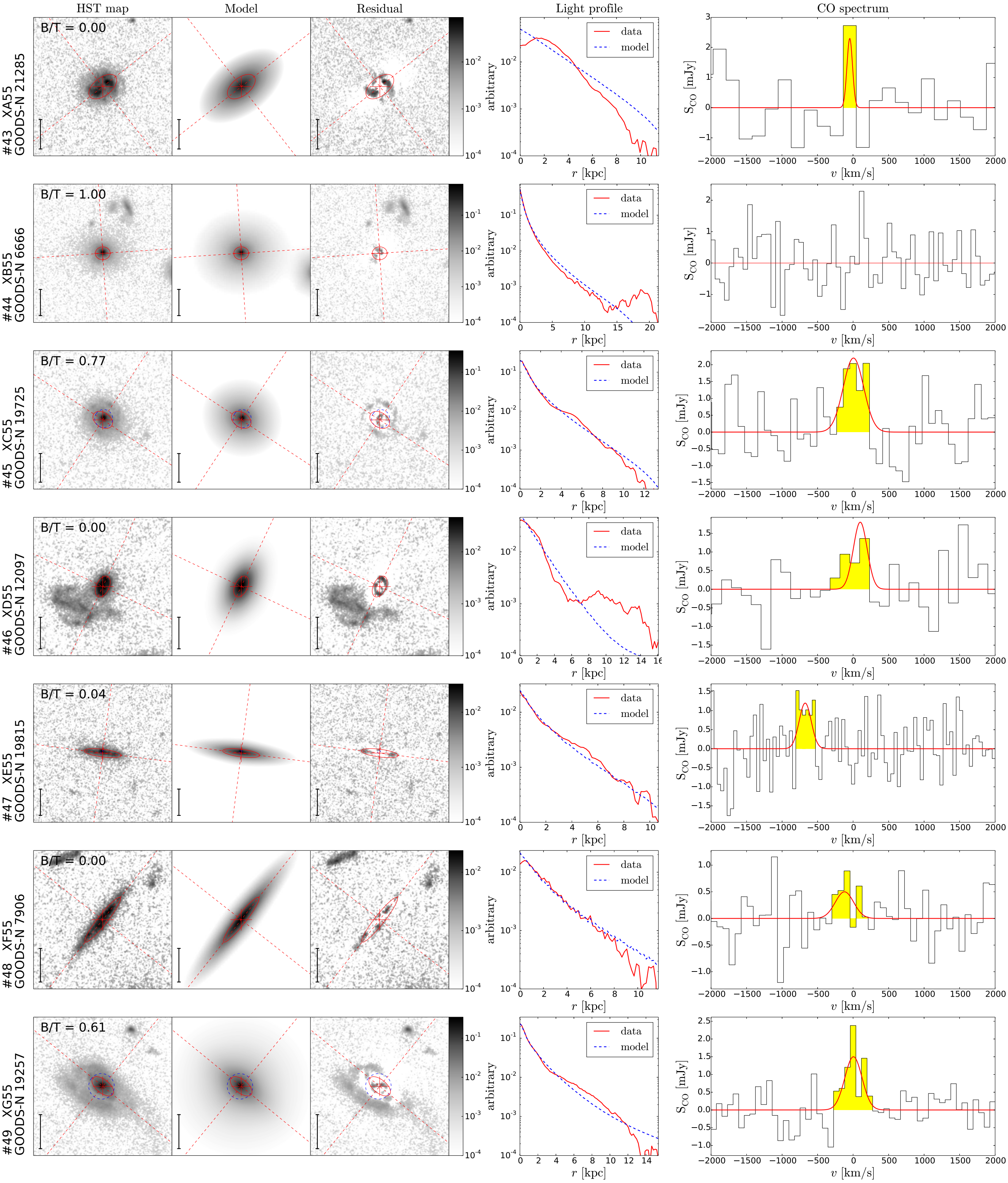
HST map
Model
Residual
Light profile
CO spectrum
#43 XA55 GOODS-N 21285
B/T = 0.00
#44 XB55 GOODS-N 6666
B/T = 1.00
#45 XC55 GOODS-N 19725
B/T = 0.77
#46 XD55 GOODS-N 12097
B/T = 0.00
#47 XE55 GOODS-N 19815
B/T = 0.04
#48 XF55 GOODS-N 7906
B/T = 0.00
#49 XG55 GOODS-N 19257
B/T = 0.61
data
model
arbitrary
r [kpc]
S_CO [mJy]
v [km/s]

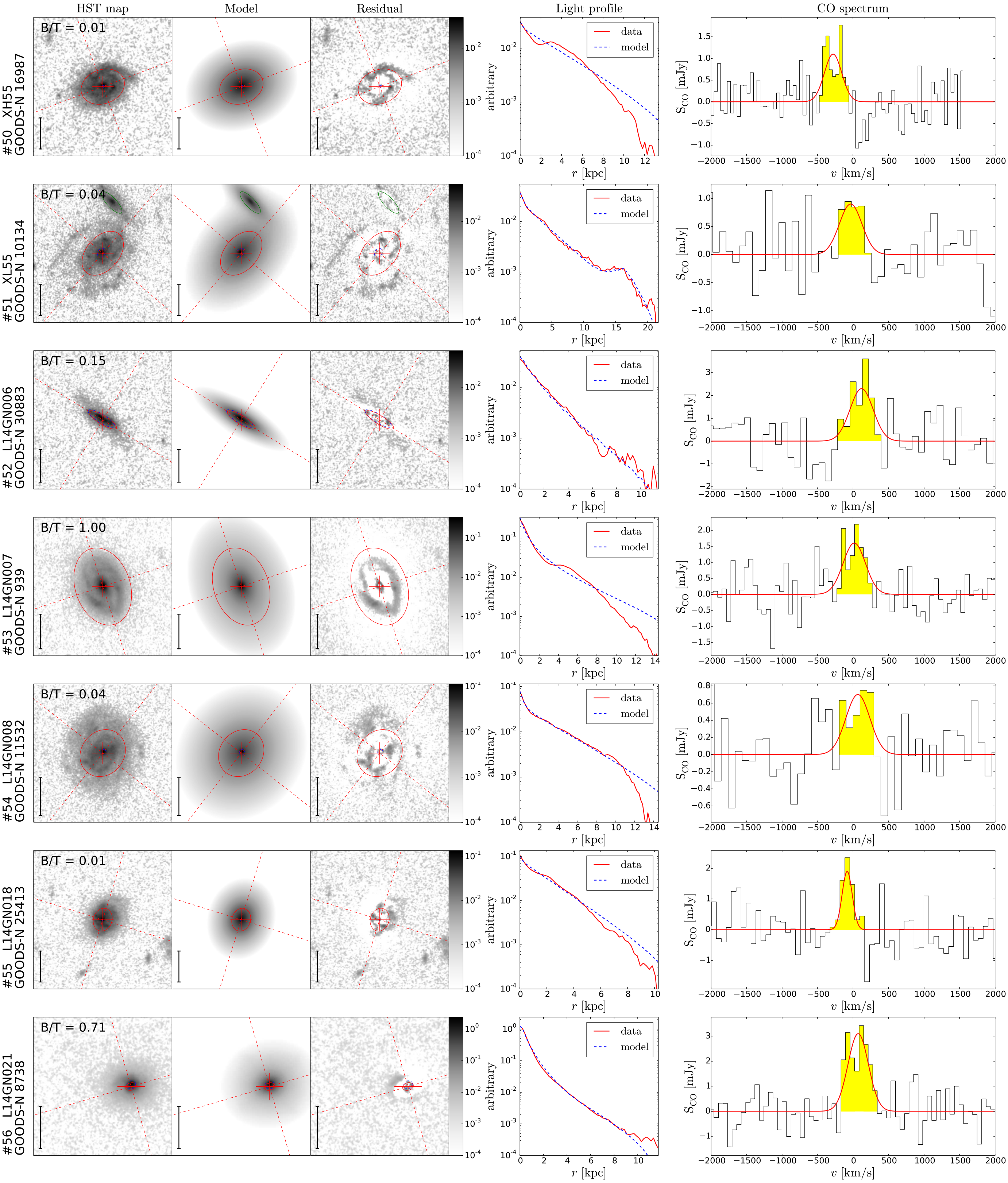
HST map
Model
Residual
Light profile
CO spectrum
#50 XH55 GOODS-N 16987
B/T = 0.01
#51 XL55 GOODS-N 10134
B/T = 0.04
#52 L14GN006 GOODS-N 30883
B/T = 0.15
#53 L14GN007 GOODS-N 939
B/T = 1.00
#54 L14GN008 GOODS-N 11532
B/T = 0.04
#55 L14GN018 GOODS-N 25413
B/T = 0.01
#56 L14GN021 GOODS-N 8738
B/T = 0.71
data
model
arbitrary
r [kpc]
S_{CO} [mJy]
v [km/s]

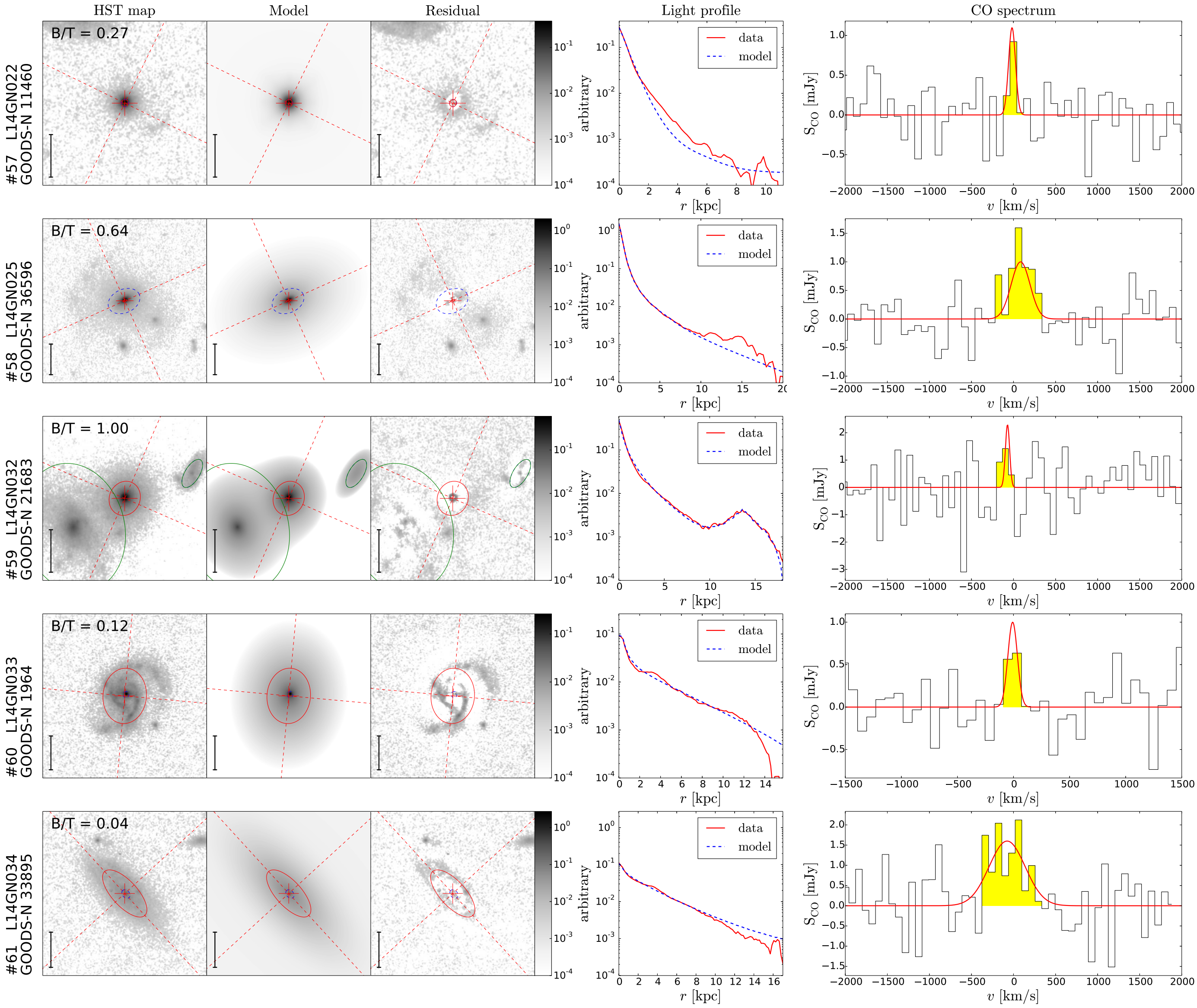
HST map
Model
Residual
Light profile
CO spectrum
#57 L14GN022
GOODS-N 11460
B/T = 0.27
#58 L14GN025
GOODS-N 36596
B/T = 0.64
#59 L14GN032
GOODS-N 21683
B/T = 1.00
#60 L14GN033
GOODS-N 1964
B/T = 0.12
#61 L14GN034
GOODS-N 33895
B/T = 0.04
data
model
arbitrary
r [kpc]
S_CO [mJy]
v [km/s]